Systematic discovery of protein interaction interfaces using AlphaFold and experimental validation

Chop Yan Lee[1,†], Dalmira Hubrich[1,†], Julia K. Varga[2,†], Christian Schäfer[1], Mareen Welzel[1], Eric Schumbera[3], Milena Đokić[1], Joelle M. Strom[1], Jonas Schönfeld[1], Johanna L. Geist[1], Feyza Polat[1], Toby J. Gibson[4], Claudia Isabelle Keller Valsecchi[1], Manjeet Kumar[4], Ora Schueler-Furman[2,*], Katja Luck[1,**]

Affiliations
1 Institute of Molecular Biology (IMB) gGmbH, 55128 Mainz, Germany.
2 Department of Microbiology and Molecular Genetics,Institute for Biomedical Research Israel-Canada, Faculty of Medicine, The Hebrew University of Jerusalem, Jerusalem 9112001, Israel.
3 Institute of Molecular Biology (IMB) gGmbH, 55128 Mainz, Germany. Current address: Computational Biology and Data Mining Group Biozentrum I 55128 Mainz, Germany.
4 Structural and Computational Biology Unit, European Molecular Biology Laboratory, Heidelberg, 69117, Germany.

*Corresponding author. Tel: +972-2-675-7094, E-mail: ora.furman-schueler@mail.huji.ac.il
**Corresponding author. Tel: +49-(0)6131-3921440, E-mail: k.luck@imb-mainz.de
†These authors contributed equally to this work.

Abstract

Structural resolution of protein interactions enables mechanistic and functional studies as well as interpretation of disease variants. However, structural data is still missing for most protein interactions because we lack computational and experimental tools at scale. We thoroughly assessed AlphaFold-Multimer accuracy for structure prediction of interactions involving folded domains binding to short linear motifs from the ELM database. The structure predictions were highly sensitive but not very specific when using small protein fragments. Sensitivity decreased substantially when using long protein fragments or full length proteins with intrinsically disordered regions. We delineated a fragmentation strategy to optimize sensitivity and applied it to interactions between proteins associated with neurodevelopmental disorders. This enabled prediction of highly confident and likely disease-related novel interfaces, but also resulted in many high scoring false positive predictions. Experiments supported predicted interfaces between CREBZF-HCFC1, FBXO23-STX1B, STX1B-VAMP2, ESRRG-PSMC5, PEX3-PEX19, PEX3-PEX16, and SNRPB-GIGYF1 providing novel molecular insights for diverse biological processes. Our work highlights exciting perspectives, but also reveals clear limitations and the need for future developments to maximize the power of Alphafold-Multimer for interface predictions.

Introduction

Protein-protein interactions (PPIs) are essential for the proper functioning of essentially all cellular processes. The last decade has seen tremendous progress in the systematic mapping of human protein interactions. Using yeast two-hybrid (Y2H) as primary screening method, more than 60,000 binary interactions between human proteins have been identified (hereafter referred to as the HuRI dataset, (Luck *et al*, 2020)). Mass spectrometry-based approaches involving affinity purification or co-fractionation have identified around 150,000 co-complex associations between human proteins (Drew *et al*, 2017; Huttlin *et al*, 2021). The systematic nature of these interactome mapping efforts enabled the discovery of protein interactions for many of the remaining poorly characterized proteins. In principle, protein interaction data enables gene function prediction and the study of genotype-to-phenotype relationships. However, to understand the molecular function of individual PPIs, co-existence or mutual exclusivity of partner proteins in protein complexes, and the effect of mutations on protein function, structural information on how these proteins interact with each other is required. Unfortunately, a structure of the complex at atomic resolution is known only for approximately 4% of the interactions detected in human binary interactome mapping efforts (Luck *et al*, 2020).

Modular proteins interact with each other using a variety of different functional elements such as stably folded domains, intrinsically disordered polypeptide regions, short linear motifs (hereafter referred to as motifs), or coiled-coil helices forming domain-domain, domain-motif, disorder-disorder, or coiled-coil interfaces for example. Resources such as 3did (Mosca *et al*, 2014) or the ELM database (ELM DB) (Kumar *et al*, 2022) collect observed contacts between domain types and domain-motif interface types, respectively. Such interface type collections can be used to predict occurrences of known interface types in protein interactions (Weatheritt *et al*, 2012; Mosca *et al*, 2013). However, it is reasonable to expect that many more ways by which proteins interact with each other remain to be discovered. This is likely particularly true for motif-mediated PPIs, which are anticipated to number in the hundreds of thousands or millions (Tompa *et al*, 2014). Motifs are short stretches of amino acids in disordered regions of proteins that usually adopt a more rigid structure upon binding to folded domains in interaction partners (Davey *et al*, 2012). Motif-mediated interactions are of moderate binding affinity and thus, are particularly suited to mediate dynamic cell regulatory and signalling events (Van Roey *et al*, 2012). However, due to the transient nature of their interactions and the disorderliness of motif-containing proteins, this mode of binding is also expected to be highly understudied. Interactome maps like the ones described above are likely a treasure trove for the discovery of novel interface types, yet, no good experimental or computational methods exist to systematically map or predict protein interaction interfaces.

The release of the neural network-based software AlphaFold (AF) was not only a breakthrough for the prediction of monomeric structures of proteins (Jumper *et al*, 2021) but multiple studies published shortly thereafter also suggested the ability of AF to predict structures of pairwise protein interactions and complexes. Sensitivities of around 70% were reported using benchmark datasets of structurally resolved protein interactions originally developed to evaluate docking methods (Akdel *et al*, 2022; Bryant *et al*, 2022; preprint:Evans *et al*, 2021; Johansson-Åkhe *et al*, 2021). Other studies focused on structures of domain-motif interfaces to specifically evaluate AF's ability to predict structures for this mode of binding reporting similar success rates (Akdel *et al*, 2022; Johansson-Åkhe *et al*, 2021; Tsaban *et al*, 2022).

Only few studies also evaluated AF's specificity for the prediction of interface structures using random protein pairs or mutation of motifs to poly-alanine stretches (Akdel *et al*, 2022; Johansson-Åkhe *et al*, 2021; Tsaban *et al*, 2022). Different studies used several different versions of AF due to fast-paced releases of newer software versions and reported on different metrics such as the model confidence, pDockQ, average interface pLDDT, iPAE, ipTM, etc, for their ability to distinguish good from bad structural models (Bryant *et al*, 2022; O'Reilly *et al*, 2023; Tsaban *et al*, 2022; preprint:Evans *et al*, 2021; Teufel *et al*, 2023). We generally lack a comprehensive assessment of the latest AF releases and metrics across different types of PPI interfaces for their sensitivity, specificity, and potential biases for the prediction of interface structures.

Going beyond the studies that used AF for the prediction of interfaces for individual protein interactions, in a landmark study researchers applied AF onto 65,000 human PPIs derived from HuRI and highly confident co-complex associations to structurally annotate the human interactome with AF-derived models. High confidence models were obtained for about 3,000 PPIs, which increased to 10,000 PPIs at a more lenient confidence cutoff (Burke *et al*, 2023). The authors noted a smaller fraction of highly confident structural models obtained for PPIs from the HuRI dataset and reported that proteins in HuRI contain more intrinsic disorder and are less conserved compared to proteins from co-complex datasets. AF model confidence scores also increased for PPIs with proteins that are less disordered and more conserved, indicating that AF predictions work less well for PPIs mediated by interfaces involving disordered regions such as domain-motif interfaces, which likely dominate the human interactome (Tompa *et al*, 2014). However, AF benchmarking studies reported similarly high success rates for domain-motif interfaces compared to general docking benchmark datasets. These discrepancies in sensitivities could be a result of two possible factors. First, they might point to differences in AF performance if small interacting fragments are used for interface prediction, as done in the benchmark studies, versus full length sequences used for structure prediction in (Burke *et al*, 2023). Second, these discrepancies could also point to difficulties of AF to predict structures of interface types involving disordered regions that have not been solved before of which there are likely many in HuRI. It remains to be addressed to what extent these two possible factors contribute to the challenges encountered specifically for domain-motif interface modeling.

Determination of accuracies of novel predicted interface structures by AF ultimately requires experimentation. AF interface predictions for individual PPIs have occasionally been experimentally corroborated (Mishra *et al*, 2023; preprint:Bronkhorst *et al*, 2023). A more systematic experimental confirmation of AF interface models has been attempted using crosslinking mass spectrometry (XL-MS) (Burke *et al*, 2023; O'Reilly *et al*, 2023). O'Reilly and co-workers reported that only a few of the crosslinks have violated distance constraints for interface models that match a stringent ipTM cutoff derived for PPIs from *Bacillus subtilis*, suggesting that most of these models are likely correct at least at the structural resolution that in-cell XL-MS can provide (O'Reilly *et al*, 2023). While in-cell XL-MS is a very elegant approach to obtain experimental information on PPI interfaces in unperturbed settings, it is still a method that is only accessible to few experts in the field. Other experimental approaches are needed, which can, ideally at high throughput, confirm structural models for PPIs. Bioluminescence resonance energy transfer (BRET) has been more recently established as a binary PPI assay that can be operated in 96 well format using transient transfections in mammalian cell lines

(Trepte *et al*, 2018). Importantly, the readout is quantitative and thus allows determination of interaction strength and fusion protein expression levels.

In this study, we thoroughly benchmarked the two most recent versions of AlphaFold Multimer (hereafter referred to as AF) for their ability to predict domain-domain and domain-motif interfaces (DDIs and DMIs). We found that prediction accuracies drop when using longer protein fragments or full length proteins for interface predictions and developed a strategy particularly suited for the prediction of novel domain-motif interfaces in human PPIs. We applied this strategy to 62 PPIs from HuRI that connect disease-associated proteins and experimentally assessed the obtained interface predictions for seven PPIs using BRET combined with site-directed mutagenesis. We identify novel interface types and report on important limitations and sources of errors in AF-derived structural models, which pave the way for future improvements in the field.

Results

Evaluation of AlphaFold on annotated domain-motif interfaces

To thoroughly assess the ability of AF to predict structures of binary protein complexes that are formed by a DMI, we extracted information on annotated DMI structures from the ELM DB (Kumar *et al*, 2022). We selected one representative structure per motif class (136 structures in total), manually defined the minimal domain and motif boundaries, and submitted the corresponding protein sequence fragments for interface prediction to AF (Fig S1A). To evaluate the accuracy of the predicted structural models, we superimposed the actual structure and predicted model on their domains and based on this superimposition, we computed the all atom RMSD between the motif of the predicted model and the actual structure (Fig S1A). We found that 35% of the structural models were so accurately predicted that even the side chains of the motif were correctly positioned while for another 32% the backbone but not the side chains of the motif were accurately predicted. For 26% of the structures the motif was modeled into the correct pocket, but in a wrong conformation, while, for the remainder of the structures, AF failed to identify the right pocket (Fig 1A). A similar performance was obtained when using the DockQ metric (Fig S1B,C, Table S1). This performance is unaltered when using or switching off AF's template function (Fig S1D,E). The use of DMI structures annotated by the ELM DB enables us to explore potential differences in AF's performance regarding motif properties. We find no significant differences in model accuracy between different categories of motif classes (two-sided Mann-Whitney test on all pairwise combinations, *n*: DEG=10, DOC=21, LIG=94, TRG=9, MOD=2, $\alpha=0.05$, test statistics of all pairwise combinations between 15 and 852, Fig 1B), secondary structure elements (two-sided Mann-Whitney test on all pairwise combinations, *n*: helix=42, strand=7, loop=87, $\alpha=0.05$, test statistics of all pairwise combinations between 184 and 2029, Fig 1C), nor by how hydrophobic, symmetric, or degenerate the motif sequence is (Pearson $r < \mathrm{abs}(0.08)$, $\alpha=0.05$ Fig S1F-H). AF models display significantly more differences to structures solved by other methods, i.e. NMR, than X-ray crystallography (two-sided Mann-Whitney test, *n*: X-ray=115, Others=21, $p < 0.01$, test statistics=811, Fig 1D) possibly because NMR structures better represent structural dynamics that AF cannot capture, since it was trained to predict the crystallized forms of proteins. The all-atom motif RMSD significantly anti-correlates with various AF-derived metrics (Pearson $r = -0.55$, p-value < 0.05 Fig S1I,J) suggesting that these metrics are indicative of good versus bad structural models and can be used for *de novo* interface predictions.

Evaluation of AlphaFold's specificity for domain-motif interfaces

The benchmarking reported in the previous section evaluated AF's sensitivity for DMI predictions when providing sequences for the minimal interacting fragments. To assess AF's specificity for this task, we generated three different random DMI datasets. First, we randomly paired domain and motif sequences from the positive reference dataset taking into account that no motif sequence was paired with a domain sequence from the domain type that the motif is known to interact with. Second and third, we mutated one and two key motif residues, respectively, to residues of opposite chemico-physical properties. Receiver operating characteristic (ROC) and precision-recall (PR) curves using the positive and random datasets (Fig 1E, Fig S2A,B, Table S2) show that the AF-derived metrics model confidence (preprint:Evans *et al*, 2021), average interface residue pLDDT, average motif interface residue pLDDT, pDockQ (Bryant *et al*, 2022), and iPAE (Teufel *et al*, 2023) discriminated well between both reference datasets when randomizing domain-motif pairs or introducing two motif mutations (max AUC 0.86). The pDockQ score performed slightly worse (AUC=0.77). However, all metrics failed when mutating only one motif residue (max AUC 0.66). Metrics such as the domain interface residue pLDDT or the number of atoms or residues predicted to be in contact with each other, discriminated poorly between all reference datasets (AUC around 0.64).

Evaluating AlphaFold's performance for the prediction of domain-domain interfaces

To evaluate whether AlphaFold performs similarly for the prediction of DDIs as it did for DMIs and whether the same metrics to discriminate good from bad structural models can be used, we used a reference dataset of 58 DDI structures that we manually curated out of random selections of domain-domain contact pairs extracted from 3did (Mosca *et al*, 2014). As a negative dataset, we randomized the pairing of these domains. Using ROC and PR statistics we found that AlphaFold performed slightly worse on this DDI benchmark dataset compared to its performance on DMIs (max AUC 0.79 vs. 0.86) (Fig 1E, Fig S2A,B, Table S2) but still showed significant discriminative power. Interestingly, the best performing metric for DDI predictions was the average interface pLDDT score, which ranked fourth for DMI predictions.

Application of AlphaFold for providing structural models for motif classes without available structural data

After evaluating the accuracy of AF to predict DMIs using minimal interacting regions, we aimed to use this setup for the prediction of structural models for motif classes in the ELM DB for which no structure of a complex has been solved yet. We identified 125 such motif classes based on ELM DB annotations (Table S3). Of those, we selected all domain-motif instances where both the motif and the domain were derived from human or mouse proteins and submitted the corresponding domain and motif sequences for structure prediction to AF. Using an average motif pLDDT cutoff of > 70, we obtained confident structural models for 21 motif classes. We manually inspected the structural models and noticed that even though these ELM classes have no annotations with structures, solved structures for an exact ELM instance or a very likely new instance for the ELM class are available for 11 out of the 21 cases, and for the rest, a close homolog structure had been solved. For example, for LIG_MYND_3 and

LIG_MYND_1, a structure solved by NMR for a LIG_MYND_2 interaction is available (Fig S2C,D). For MOD_SUMO_rev_2, a structure of a reversed motif is available (and annotated as such in the MOD_SUMO_for_1 class). Here it is interesting to see how very dissimilar binding modes (flexible for MOD_SUMO_for_1, helical for MOD_SUMO_rev_2), are still able to place the important binding residues in the same pockets (Fig 1F). Finally, for CLV_C14_Caspase3-7, the structure of the caspase bound to peptide-like inhibitors has been solved (e.g. PDB:1F1J, PDB:5IAN, PDB:6KMZ), and structures of more distant caspases bound to a cleaved peptide substrate are also available. For proteases, one great advantage of AF is the ability to model both the catalytically active enzyme and an uncleaved substrate, which is practically impossible to solve experimentally (Fig 1G).

Finally, LIG_HCF-1_HBM_1 describes a motif class in the ELM DB that is bound by the N-terminal beta-propeller Kelch domain of HCFC1 consisting of six Kelch repeats. Kelch domains have been shown to bind to motifs at a number of different sites, and thus, without prior knowledge, it is difficult to determine where the HCFC1-binding motif (HBM) would bind. HCFC1 is a transcription factor that associates with other transcription factors (Lu *et al*, 1997), splice factors (Ajuh *et al*, 2002), and cell cycle regulators (Freiman & Herr, 1997; Machida *et al*, 2009). The motif with the pattern [DE]H.Y consists of three very conserved positions. We generated AF models of high confidence for the HCFC1 Kelch domain interacting with multiple motif instances that are annotated in the ELM DB. All complexes show the tyrosine of the motif docked into a deep pocket at the bottom/top of the Kelch domain (Fig 1H,I and Fig S2E-G), with slight variations in how the tyrosine is exactly positioned in the pocket (Fig S2E-G). Based on clone availability we selected the structural model between HCFC1 and CREBZF for experimental validation. For this purpose, we used a BRET protein interaction assay that is based on transient overexpression of two proteins in HEK293 cells (Trepte *et al*, 2018). Both proteins are expressed as fusion constructs either to the Nanoluc luciferase (the donor) or mCitrine (the acceptor). Interaction of both proteins results in a BRET from the oxidized substrate of the donor to the acceptor molecule, if both are close enough to each other for the BRET to occur (see Methods for details). We observed significant binding and BRET saturation when assaying wildtype CREBZF and HCFC1 proteins (Fig 1J and Fig S2H,I). Mutation of the [DE]H.Y motif tyrosine to alanine (Y306A) or mutation of two residues in the Kelch domain pocket (L257F, L138F), which are predicted to be in contact with the motif tyrosine or histidine residue (Fig 1I), strongly reduced BRET signals indicating weakening or loss of binding (Fig 1J and Fig S2H,I). A pathogenic mutation (S225N, source ClinVar (Henrie *et al*, 2018)) close to the pocket did not result in loss of binding (Fig 1J and Fig S2H,I). In accordance, no assertion criteria for the annotation of this mutation to be pathogenic is provided by ClinVar. Collectively, these experimental results support the structural models of the HCFC1 Kelch domain pocket - motif interaction.

Evaluation of AlphaFold’s ability to predict interfaces in full length proteins

Most PPIs known to date have been identified using full length protein sequences in systematic interactome mapping efforts. For the vast majority of these PPIs, no fragment or interface information is available. Thus, the question emerges how AF would perform on DMI predictions when longer protein sequences or full length proteins are submitted. To answer this question we selected 31 DMI structures from the positive reference dataset used above and generated random domain-motif pairs of those as negative control. The selected structures were sampled from different prediction accuracy categories (Fig 1A, Table S4). We then gradually extended the motif and domain sequences by first adding flanking disordered regions, then neighboring folded domains before using the full length sequences (Fig 2A). Comparison of the motif RMSD computed for extended versus minimal domain-motif pairs from the positive reference dataset revealed that the addition of flanking disordered regions on the motif or domain side sometimes slightly improved prediction accuracies while the addition of neighboring structured domains or the use of full length sequences led to a significant worsening of model accuracies (Fig 2A). Interestingly, despite the fact that for smaller extensions model accuracies remained the same or slightly improved as determined by motif RMSD, AF-derived metrics such as the model confidence or average motif interface residue pLDDT gradually dropped with increasing fragment length (Fig 2B, Fig S3A-C). ROC plots of predictions for a benchmark consisting of the positive and random domain-motif pairs revealed that upon extension the optimal cutoff of model confidence and iPAE considerably changed as well (Fig 2C, Fig S3D,E, S4A Table S5). This means that different model confidence or iPAE cutoffs are to be used depending on the length of the submitted protein sequences, which is rather impractical and thus disfavors both metrics for DMI predictions. The average motif interface residue pLDDT metric appeared to be more robust with respect to fragment length.

Extending motif sequences for interface prediction with AlphaFold reveals important motif sequence context

Various studies have highlighted that flanking sequences of motifs can influence binding affinities and specificities (Luck *et al*, 2012; Bugge *et al*, 2020). Motif annotations in the ELM DB usually refer to the core sequence of the motif, often because information on putative roles of flanking sequences is missing. In the previous section, we observed that some motif extensions notably improved AF prediction accuracies. In the hope that these cases would point to motifs with important sequence context, we manually inspected eight predictions for which the motif RMSD decreased by more than 1 Å when extending the minimal motif sequence once to the left and right by the length of the motif (extension step 1 in Fig 2A,D). By doing so interesting patterns emerged: The most prevalent contribution to increased prediction accuracies is the stabilization of the secondary structure of the motif (Fig 2E, Fig S4C) contributed by both sidechain and backbone atoms in the flanking regions, as shown for the interaction involving the motif LIG_CAP-Gly (Fig 2E). For the LIG_NBox_RRM motif, AF placed a part of the domain into the binding pocket rather than the motif, although the motif had the correct helical conformation. Elongation of the motif extended this helix, thereby increasing the interaction surface and eventually pushing out the domain's tail from the pocket (Fig 2F). This fits with other reports where AF has been shown to predict preferential binding of competing motifs (Chang & Perez, 2023). For the LIG_HOMEOBOX class prediction, the motif is positioned in the wrong pocket unless flanking regions are included (Fig S4C). For DOC_MAPK_JIP1, motif extension results in an extended motif conformation and consequently in a structural model with lower overall RMSD (Fig S4C). For the LIG_GYF class, most models converge into an inverse orientation of the backbone except for one of the extended motifs, which lies in the binding pocket in the correct orientation (Fig S4C). A further interesting case is the DOC_USP7_UBL2 motif, for which the AF models provide different suggestions as to the binding orientations of a repeated motif. When using the isolated motif, the prediction converges onto one conformation of a motif backbone very similar to the solved crystal structure, but positioned in the opposite orientation. When modeling the extended region that includes another copy of the motif, various conformations in the correct orientation are generated, resulting in lower but still high RMSD, and less convergence (Fig 2G). In this case, it might well be that several of these conformations would be possible, and indeed, the solved structure of the complex of the full PPI suggests that the loop containing this repeated motif is long enough to allow for binding in two different orientations. In summary, these analyses point to motif classes whose sequence boundaries could be refined. Interestingly, for a motif instance from the LIG_BIR_III_2 class, slight motif extensions actually led to a substantial decrease in prediction accuracy. In this case, the motif is located at a neo-N-terminus that is only revealed after cleavage of the protein by a caspase (Fig S4D). When the motif is extended in the context of the full length protein, the correct placing of the N-terminus of the motif becomes physically impossible, pushing the motif out of the pocket. This highlights the importance of incorporating knowledge about sequence context while modeling and interpreting AF predictions.

Comparison of AlphaFold v2.2 with v2.3

During the course of our work, AF multimer version 2.3 was released. To determine whether the new release improved DMI prediction accuracies, we repeated all benchmarking with AF v2.3 and found that motif RMSDs and other AF-derived metrics on average improved compared to AF v2.2 when using minimal interacting fragments (Fig S5A-D, Table S1, two-sided Wilcoxon signed-rank test on motif all atom RMSD: n=136, W=2413, $p < 0.0001$). AF v2.3 still showed a decrease in prediction accuracy when using extended protein fragments but this decrease was less pronounced compared to the corresponding decrease for v2.2 (Fig S5E,F, Table S4). Despite these improvements on the sensitivity side of AF, when benchmarked against random datasets, overall prediction accuracies only slightly improved compared to v2.2 (Fig S5G,H, Fig S6A-C, Table S2,S6).

Application of AlphaFold for the discovery of novel interfaces in protein interactions without any a priori interface information

Since the use of larger or full length protein sequences leads to a poor sensitivity for DMI predictions by AF, we devised the following strategy for the use of AF for interface predictions for known protein interactions: Using AF models of the full length monomeric structures of both interacting proteins, we decided on boundaries between structured domains and disordered regions based on manual inspection. This was necessary because testing available code developed for this purpose, like clustering using the PAE matrix, turned out to be too inaccurate because erroneous removal of flanking residues that are still contributing to the folding of a structured domain can heavily mislead AF predictions. We then fragmented the disordered regions by designing overlapping fragments varying in length from ten residues up to the length of the respective disordered region (Fig 3A). We then paired disordered with ordered, and ordered with ordered fragments for interface prediction by AF (Fig 3A). To assess to which extent this fragmentation approach would lead to an increase in false model predictions, we selected 20 out of the 31 DMI structures that were previously used to investigate the effect of fragment extension on prediction accuracies. We made 20 random pairings of domain and motif proteins, fragmented these proteins, and submitted all fragment pairs for interface prediction with AF. As expected from an earlier estimated 20% false positive rate (FPR) (Fig S4A), 19 of the 20 random protein pairs had at least one fragment pair that produced a model above the cutoff (Fig 3B, Table S7). The fraction of fragment pairs that scored above the cutoff varied from 0% to 15.7 % (Fig 3B, Table S7) indicating that predictions done using this fragmentation approach will produce a considerable number of false models.

We selected PPIs from HuRI that connect proteins associated with neurodevelopmental disorders (NDDs) and subjected these to our AF fragmentation pipeline to predict putative DMIs and DDIs. Out of a total of 67 PPIs, we modeled 62 (5 were too large), and for 51 PPIs we obtained at least one structural model of significant confidence (Fig 3C,D). In retrospect, manual inspection of the predictions obtained for these PPIs revealed that for 9 PPIs a solved structure of the interface was already available. Reassuringly, six out of these were accurately predicted by AF. For the remainder of the PPIs, 12, 16, and 14 resulted in a likely correct, questionable, or likely wrong prediction, respectively (Fig 3C,D, Table S8, Text S1). Of note, for 8 of the 12 PPIs with a likely correct prediction, AF predictions performed using the full length proteins (Burke *et al*, 2023) did not result in a high confidence prediction (Fig 6E), highlighting the importance to use smaller protein fragments for interface predictions. Based on clone availability, we selected 49 of the 62 PPIs for experimental validation of the predicted interfaces using the BRET assay introduced earlier. For 30 of the 49 selected PPIs for experimental testing we obtained sequence-confirmed clones with luciferase and mCitrine fusions. For 28 of these PPIs both partners were expressed in our experimental system as determined by total luminescence and fluorescence measurements (Fig 3D,F). These 28 PPIs were thus amenable for experimental testing. Significant BRET signals were observed for 11 of these 28 PPIs (Fig 3F). Of those, 7 PPIs were selected for mutation design and interface validation (Fig 3D,F). The remaining four PPIs were not further considered because for three of them a structure already exists (CSNK2B-CSNK2A1, PNKP-XRCC4, UBA5-GABRAPL2) and for the fourth interaction (KCTD7-CUL3) we classified the predicted interface as likely wrong. In the following, we will describe for the seven selected PPIs the structural models that we obtained, the experimental results aimed at validating or disproving the predictions, and how this aligns with published work starting with the least and ending with the most exciting findings.

TRIM37 and PNKP

TRIM37 is a RING domain-containing E3 ligase known to regulate centriole reduplication, transcriptional repression, and peroxisome import (Kallijärvi *et al*, 2005; Bhatnagar *et al*, 2014; Wang *et al*, 2017). PNKP has dual phosphatase and kinase activity that it uses to modify broken DNA strands preparing them for repair (Aceytuno *et al*, 2017; Jilani *et al*, 1999). Both proteins showed clear signs for interaction in the BRET assay (Fig 3F). AF predicted the PNKP FHA domain to bind to several disordered stretches in TRIM37 (Fig 4A) that are overall negatively charged. These short regions were predicted to bind to a pocket on the FHA domain that is known to bind phosphorylated threonines (Durocher *et al*, 2000), which led us to conclude that these predictions were likely wrong. AF also predicted the MATH domain of TRIM37 to bind to two separate disordered putative motifs located between the FHA domain and phosphatase domain in PNKP (Fig 4A-C). In particular, the motif ranging from 110-116 attracted our attention because phosphorylation of S114 has been reported to stabilize PNKP protein levels (Parsons *et al*, 2012). We hypothesized that S114 phosphorylation might hinder binding of TRIM37 to PNKP and subsequent ubiquitylation. To confirm the accuracy of this predicted interface we assayed binding of PNKP S114D and P112R as well as TRIM37 F328R and N376R mutants for loss of binding to the wildtype partner protein (Fig 4D, S7A). BRET titration curves show a titration behavior where reproducibly for high acceptor to donor ratios, a sudden increase in BRET signal is observed, hindering a fit and proper BRET50 estimation (Fig 4D). Regardless, none of the mutants showed a decrease in BRET signal compared to wildtype indicating that TRIM37 and PNKP do not interact with each other via this interface.

PSMC5 and ESRRG

PSMC5 is a subunit of the 19S regulatory complex of the 26S proteasome. It has been shown previously that PSMC5 is recruited to promoters of nucleic acid receptor target genes and to interact with the nucleic acid receptor RARA thereby regulating transcription (Ferry *et al*, 2009). Interestingly, in HuRI, PSMC5 was found to interact with RARA and RARB as well as with other nuclear receptors such as ESRRG, RORB, and RORA. AF predicted with high confidence two different supposedly disordered motifs in PSMC5 to dock into the NR-box pocket of the hormone receptor domains of ESRRG, RORB, and RARB (Fig 4E-G). Hormone receptor domains bind LxxLL motifs (LIG_NRBOX class in ELM DB). In our BRET system, we could detect the interaction between PSMC5 and ESRRG (Fig 3F), and selected both putative motifs in PSMC5 as well as residues in the domain pocket of ESRRG for single point mutagenesis (Fig 4F,G). Of note, the first motif located N-terminal to the AAA domain in PSMC5 is predicted by AF with modest confidence to make intramolecular contacts with the AAA domain. These contacts are also observed in solved structures of the proteasome (i.e. PDB:5VFT (Zhu *et al*, 2018)). The second motif is at the very C-terminus of PSMC5 and carries a tryptophan, which is much more bulky compared to leucine residues usually observed to bind NR-box pockets. In line with these critical observations, we reproducibly found that none of the motif mutations decreased binding to ESRRG compared to wildtype PSMC5 while both domain pocket mutations led to a remarkable reduction in BRET signal (Fig 4H, S7B,C) indicating that PSMC5 might bind to ESRRG via this pocket but not with the predicted motifs.

STX1B, FBXO28, and VAMP2

We were able to confirm binding between STX1B and FBXO28 as well as between STX1B and VAMP2 in the BRET assay (Fig 3F). STX1B (OMIM:616172) and FBXO28 (OMIM:619777) are associated with epileptic phenotypes while mutations in VAMP2 (OMIM:618760) lead to NDD phenotypes with autistic features. Specific cellular functions of FBXO28 are unknown but because of the presence of an Fbox domain, it is supposed to function as an SCF E3 ligase in the ubiquitin-proteasome pathway. AF predicted multiple modest confident interfaces between STX1B and FBXO28 involving disordered regions in STX1B or FBXO28 and a coiled-coil interface between the extended helix of FBXO28 and the SNARE domain of STX1B (Fig 5A,B). AF also predicted a coiled-coil interface between STX1B and VAMP2 of modest confidence (Fig 5A,C). STX1B is a close homolog to STX1A. STX1A is a subunit of the SNARE complex together with VAMP2 and SNAP25 mediating fusion of synaptic vesicles with the presynaptic plasma membrane. The complex between STX1A, VAMP2, and SNAP25 has been solved structurally and shows a 4-helix bundle with a 1:1:2 stoichiometry, respectively (PDB:1N7S (Ernst & Brunger, 2003)). This structure together with our predictions suggest that STX1B might bind VAMP2 in a similar way. Indeed, removal of the SNARE domain in STX1B led to complete loss of binding to VAMP2 (Fig 5D, S8A,B). The same deletion construct or removal of the extended helix in FBXO28 also reproducibly reduced, but did not abolish, BRET signals for the STX1B-FBXO28 interaction supporting a coiled-coil interface between both proteins (Fig 5E, S8C,D). We identified three pathogenic or likely pathogenic mutations in the SNARE domain of STX1B in ClinVar of which V216E and

G226R are associated with generalized epilepsy with febrile seizures plus, type 9. Testing all three mutations in the BRET assay we observed a drastic decrease in binding to FBXO28 for STX1B V216E (Fig 5F, S8C,D). However, the effect of the mutations on the interaction with FBXO28 does not correlate with their location at the predicted interface with FBXO28 where STX1B V216E for example, is not predicted to be in contact with residues of FBXO28 (Fig 5B). This indicates that the actual predicted orientation of the two extended helices with respect to each other is likely incorrect.

Do these PPIs also involve contributions from DMI interactions? The fact that the above mentioned deletion of the extended helix in FBXO28 or the SNARE domain in STX1B reduced but did not abrogate binding of both proteins to each other (Fig 5E) suggests that a secondary interface might exist. To test this hypothesis we designed mutations aimed at disrupting two predicted DMIs between STX1B and FBXO28 (named i and ii in Fig 5A). Using the BRET assay, we observed a decrease in BRET signal for a mutation on the helical bundle domain of FBXO28 predicted to bind to the N-terminal motif in STX1B (Fig S8E-H). However, mutation of the motif did not result in any loss of binding (Fig S8E-H). Mutations aimed at disrupting interface ii did not result in any loss of binding (Fig S8I-L). Interestingly, the pathogenic mutation R348L in FBXO28 predicted to be at interface ii seemed to increase binding to STX1B (Fig S8I-L). Overall, our experimental data indicate that multiple regions of FBXO28 and STX1B may be involved in the binding but the structural details of this interaction remain to be elucidated.

PEX3, PEX19, and PEX16

Peroxisomes are single membrane-bound organelles that function in amino acid and lipid biosynthesis as well as in the regulation of reactive oxygen species. Peroxisomes mediate these functions via peroxisomal membrane proteins (PMPs) and proteins in the peroxisomal matrix (Islinger *et al*, 2018). Peroxisome homeostasis is regulated by peroxin (PEX) proteins, two of which, PEX3 and PEX19, were shown to have essential roles in this process. PEX3 is a peroxisome membrane-bound protein, which serves as a docking site for PEX19 (Fujiki *et al*, 2006). PEX19 in turn is believed to be a cytosolic carrier for PMPs to the peroxisome (Fujiki *et al*, 2006). Studies suggested two distinct interfaces between PEX19 and PEX3, one of which, believed to be the dominant one, was crystallized and is described in the ELM DB as an interaction between an N-terminal motif in PEX19 that binds to the cytosolic alpha-helical domain of PEX3 (PDB:3MK4, (Schmidt *et al*, 2010)). A monomeric model of PEX19 predicted by AF shows a disordered N-terminal tail with six isolated alpha helices, the first one corresponding to the known PEX3-binding motif. AF is known for its tendency to predict the bound conformation of disordered regions in their monomeric state, suggesting that at least some of the other isolated helices might represent sites for interaction. Indeed, AF interface predictions for various isolated PEX19 fragments when paired with the PEX3 domain identified highly confident interface predictions involving either the known PEX3-binding motif or helix 3, 5, or 6 (Fig 5G). The interaction between the known motif in PEX19 and the cognate PEX3 pocket is highly similar to the solved structure (Fig S9 A,B). Interestingly, isolated helix 5 and 6 are predicted to dock to a distal site on PEX3 while helix 3 is predicted to bind to the known docking site for the PEX19 N-terminal motif. When using the full disordered N-terminal tail of PEX19 (1-170), AF predicts the known PEX3-binding motif and helix 4 and 5 to dock into the primary and secondary pocket, respectively (Fig 5H). In Burke et al, AF predictions using both full length proteins resulted in a less confident complex prediction (average interface pLDDT=72 compared to 87) with helix 4 and 5 being docked differently into the second binding site (Burke *et al*, 2023). We introduced mutations in the known PEX19 motif and PEX3 pocket (Fig S9A) and found, using the BRET assay, that F29K in the known PEX19 motif weakens but clearly maintains binding, supporting the notion of a second binding site (Fig 5I, S9C,D) while also highlighting the sensitivity of the BRET assay. Unfortunately, L107D in PEX3 did not express while T90Q in PEX3 did not alter binding to PEX19 (Fig 5I, S9C,D).

PEX16 was suggested to serve as an integral membrane-bound receptor for PEX3 (Matsuzaki & Fujiki, 2008). However, from a structural point of view, the interaction between PEX3 and PEX16 is less well understood. The monomeric AF model of PEX16 shows a helical fold, which could in its entirety be transmembrane (TM). Between the putative TM helix 4 and 5 there is a large loop (132-214), which was predicted by AF with very high confidence to bind to a third pocket on the PEX3 domain, opposite to both binding sites mentioned earlier for PEX19 (Fig 5G,H,J). Of note, different fragments of this loop as well as the entire PEX16 were repeatedly predicted to bind in similar modes to PEX3 further increasing the confidence in this prediction. Encouraged by these results, we submitted all three full length PEX sequences for complex prediction to AF and obtained a model that supports simultaneous binding of PEX16 and PEX19 to PEX3 (Fig S9E). We individually mutated two residues in the PEX16 loop, deleted the loop in its entirety (del162-192), and mutated two residues on PEX3 (highlighted in Fig 5J). Unfortunately, higher expression levels of PEX16 seem to trigger degradation of PEX3 (Fig S9F), which we did not observe for the same constructs when co-expressed with PEX19 (Fig S9G). As a consequence, we could not obtain titration curves and BRET50 estimates but obtained reliable BRET signals for lower PEX3-PEX16 DNA transfection ratios showing that the deletion as well as both PEX3 mutants significantly decreased binding to PEX16 (Fig 5K, S9H). Of note, these PEX3 mutants (R54S and E272R) did not alter binding to PEX19 showing that the overall structural integrity of PEX3 was not perturbed by these mutations (Fig 5I, S9D).

Combining all structure prediction and experimental results with previously published work on the three PEX proteins, a model for a trimeric complex emerges (Fig 5L) where PEX16 fully inserts into the peroxisome membrane via a fold that consists of seven helices (residues 19-286) with its N-terminal end being cytosolic and its C-terminal end protruding into the peroxisome. The extended loop between TM helix 4 and 5 reaches into the cytosol and docks onto PEX3, which is further anchored into the peroxisomal membrane via its N-terminal TM helix (residues 13-45). PEX19 docks onto PEX3, opposite to where PEX16 is bound, via two interaction surfaces - one corresponding to the known PEX3-binding motif in PEX19 and a second one likely corresponding to a novel motif (residues 99-146) docking at a hitherto unknown second binding site on PEX3 for PEX19. This model explains how PEX3 is anchored to the peroxisomal membrane via PEX16 and how PEX3 can bind very tightly PEX19, which can then deliver PMPs to the peroxisome. Mutations in any of the three PEX proteins are associated with severe developmental phenotypes referred to as peroxisome biogenesis disorders (Fujiki *et al*, 2022). The vast majority of the around 150 mutations annotated for the three proteins are uncharacterized (Henrie *et al*, 2018), dozens of which fall into the predicted interfaces. The structural models obtained from this work can inform future studies aimed at characterizing the effects of these mutations.

SNRPB and GIGYF1

SNRPB is one of seven Sm proteins that together form a heptameric ring, which binds small nuclear RNA. They form the core for four of five small nuclear ribonucleoprotein complexes that mediate mRNA splicing. The heptameric ring is formed via interactions between the LSM domains that occur at the N-terminus of each Sm protein. Sm proteins are generally small (less than 100 amino acids) with the majority of them only consisting of the LSM domain. SNRPB's protein architecture is special in that it contains a disordered C-terminal tail of around 140 residues. This disordered region is particularly rich in prolines and glycines and has been shown previously to bind to the OCRE domain of RBM5 (Mourão *et al*, 2016). In HuRI, an interaction was detected between SNRPB and GIGYF1. GIGYF proteins are associated with functions such as mRNA degradation, translational repression, mRNA decapping, and miRNA-mediated gene silencing (Sobti *et al*, 2023). GIGYF1 contains a GYF domain. GYF domains are generally known to bind proline-rich motifs as also annotated in the ELM DB (LIG_GYF). However, current motif annotations denote conserved positively charged residues surrounding a stretch of four consecutive prolines. This pattern does not match the SNRPB protein sequence. AF predicted with high confidence multiple disordered regions in the C-terminal region of SNRPB to bind to the GYF domain of GIGYF1 (Fig 6A,B). Interestingly, these putative motifs repeatedly displayed the sequence PPPGM(R). AF also predicted with similar confidence binding of the LSM domain to various fragments in the long disordered regions of GIGYF1 (Fig 6A). These regions did not display any common sequence pattern. Comparison with a solved structure of the Sm complex (PDB:4WZJ, (Leung *et al*, 2011)) revealed that these sequences were docked onto the LSM domain where neighboring LSM domains of other Sm proteins would bind SNRPB as part of the heptameric Sm complex (Fig 6C). We thus conclude that these predictions are likely wrong. We focused on interface predictions involving the GYF domain of GIGYF1 and the C-terminal region of SNRBP. During the course of these studies, a structure was published (PDB:7RUQ, Sobti *et al*, 2023) showing binding of the GYF domain of GIGYF1 to a motif of sequence PPPGL of the protein TNRC6C confirming the binding mode predicted by AF where a hydrophobic residue (M or L) inserts into a hydrophobic pocket and where the proline residues contact the surrounding domain surface (Fig 6B,D). Of note, this hydrophobic pocket does not exist in the previously solved structure of the GYF domain of CDBP2 binding to a proline-rich peptide (PDB:1L2Z, (Freund *et al*, 2002)). Encouraged by these findings, we designed various deletion constructs of SNRPB that would gradually remove more and more of the repeated proline-rich motif and observed, using the BRET assay, that these deletion constructs gradually decreased binding to GIGYF1 (Fig 6E, S10A,B). We also mutated the GYF domain pocket and found that W498E but not L508F would decrease binding to SNRPB (Fig 6E,F, S10A-D). This was further corroborated in a co-immunoprecipitation experiment, where endogenous GIGYF1 interacted with HA-tagged full-length SNRPB (Fig 6G). This interaction appeared less pronounced upon truncation of the C-terminal proline-containing region of SNRPB (Fig 6G). This further suggests that both proteins interact with each other in cells and that this interaction is stabilized by the predicted interface.

Discussion

In this study we have investigated the ability of AF to model domain-motif interactions on a large scale using as reference annotations from the ELM DB. We were interested on the one hand in a robust assessment of AF performance for this modeling task, and on the other hand in our ability to reveal new insights on characterized as well as uncharacterized DMIs and the PPIs that they reflect. Our study allowed us to line out successes as well as the limitations of the currently leading Deep Learning tool AF. Using minimal interacting regions of curated DMI structures from the ELM DB, we obtained sensitivity estimates for AF of around 80%, which is similar compared to previously published work (Tsaban *et al*, 2022; Johansson-Åkhe *et al*, 2021). However, contrary to some earlier reports, we did not observe any significant differences in AF performance between various motif characteristics (Tsaban *et al*, 2022; Akdel *et al*, 2022). Our DMI benchmark dataset almost exclusively consisted of structures that AF has seen in the training process. Interestingly, benchmark studies done with unseen structures reported similar sensitivities (Bret *et al*, 2023) indicating that AF is not strongly biased towards structures it has seen before. We thoroughly investigated AF's FPR using random domain-motif pairs and found it to be around 20%. However, asking AF to discriminate binders from non-binders when motif sequences carried one disruptive mutation, we found that prediction accuracies were close to random. This points to an important limitation in AF's ability to predict binding specificities and is in line with previous reports on AF's inability to predict the effect of mutations (Buel & Walters, 2022). Comparison of different metrics to discriminate good from bad structural models using either minimal interacting fragments or extensions revealed the average interface pLDDT for DDI models and the motif interface pLDDT for DMI models to be the most robust and highest performing metric. However, when manually inspecting AF predictions we found it useful to consider multiple metrics, suggesting that in the future a combination of different metrics might be even more powerful to discriminate good from bad structural models. Interestingly, the number of residues or atoms predicted to be in contact with each other was poorly predictive, in contrast to a previous report (Bryant *et al*, 2022), confirming our observations that AF will always put both chains in contact with each other to create atomic contacts, and from visual inspection alone it is very challenging to tell good from bad structural models apart. We applied AF to annotated DMI instances from the ELM DB for which information on the minimal interacting fragments exists but no structural details, and obtained highly confident structural models for 21 out of 30 motif classes, one of which we experimentally validated. AF predictions can thus further enrich annotations for motif classes from the ELM DB. More work is needed to develop benchmark datasets of coiled-coil and disorder-disorder interfaces to also evaluate AF's performance for these modes of binding.

We extensively explored the influence of protein fragment length on AF's performance and found that slight extensions of minimal motif sequences can improve prediction accuracies. Inspection of individual cases revealed novel information on important motif sequence context that was so far missing in corresponding motif entries at the ELM DB. Slightly longer motif sequences seem to enable AF to build multiple sequence alignments for these fragments, thereby improving prediction accuracies in some cases. However, longer disordered fragments or fragments containing ordered and large disordered regions generally decrease AF prediction accuracies as also reported in a recent preprint (preprint:Bret *et al*, 2023). Furthermore, optimal cutoffs for various metrics such as the model confidence decreased when using longer protein fragments, making them less robust for interface prediction with AF. When evaluating performance differences for longer and shorter protein fragments we identified three DMI pairs involving the motif classes DEG_APCC_KENBOX_2, LIG_Pex14_3, and LIG_GYF, for which, during fragment extension, a second known motif occurrence was added to the fragment. This second motif was selected by AF during interface prediction, displacing the original motif and leading to a high RMSD score. We removed these instances from the dataset when evaluating AF's performance on fragment extension but they point to biologically correct variability in AF prediction outcomes due to existing multivalency of many DMIs in protein interactions. Other work suggested that AF is able to select the stronger binder among two motif occurrences (Chang & Perez, 2023), which might at least in some cases guide AF motif selections. However, in other cases this motif preference might also hinder discovery of multivalency in PPIs. For example, the use of smaller protein fragments for the protein pair SNRPB and GIGYF1 enabled the discovery of a proline-rich repeat motif in SNRPB.

In comparison to predictions made using full length proteins (Burke *et al*, 2023) we found that protein fragmentation increased the probability of obtaining a high confident interface prediction, especially for cases involving proteins with long disordered regions such as GIGYF1. For smaller and more globular proteins like the PEX proteins studied above, full length predictions can identify the right binding sites but these can be further substantiated by running additional predictions with smaller fragments. The fragmentation approach increases the number of prediction runs per protein pair from one to a couple hundred, depending on the length and modularity of both proteins. The vast majority of these fragment pairs should not interact. With a FPR of 20%, this means that in absolute terms more actual non-interacting fragment pairs will result in a prediction that makes the cutoff compared to actual interacting fragments. A big challenge is thus to identify likely correct interface predictions among all those that made the cutoff. This is also illustrated by the prediction results that we obtained for the seven protein pairs that we followed up experimentally. Clearly, AF's general limited specificity contributes to these false predictions. We observed that additional sources of error can arise from exposed intramolecular binding sites resulting from fragmentation, incorrectly designed boundaries of folded regions, and docking of protein fragments into enzymatic pockets of metabolic enzymes or sites for metal ion, DNA, or RNA binding. AF's high sensitivity with respect to intramolecular binding sites and wrongly fragmented folded regions will make it particularly hard to fully automate the fragment design process. Despite these challenges we found that recurrent interface predictions from overlapping fragments can help gain confidence in predictions, as also highlighted in a recent preprint (preprint:Bronkhorst *et al*, 2023), since we rarely observed this recurrence for likely wrong predictions.

Given the reported uncertainties in AF predictions, even for high confidence cutoffs, experimental validation is essential. The BRET assay used here has been shown in previous studies to be sensitive enough to quantify weakening of binding introduced by point mutations and to detect motif-mediated PPIs (Ebersberger *et al*, 2023; Trepte *et al*, 2018; Mo *et al*, 2022). Using the BRET assay, we were able to detect 11 out of 28 PPIs from the HuRI dataset. This retest rate is actually higher compared to retest rates of gold standard PPI datasets used in the past to benchmark various binary PPI assays including this BRET assay, attesting the overall detectability of PPIs from HuRI (Braun *et al*, 2009; Trepte *et al*, 2018; Choi *et al*, 2019). Further increases in retest rate can be obtained by testing all possible combinations of N- and C-terminal fusions to the NanoLuc luciferase and mCitrine (preprint:Trepte *et al*, 2021; preprint:Trepte *et al*, 2023). Comparison of BRET50 estimates from titration curves is conceptually the best way to assess differences in binding strengths between PPIs. However, in some cases we could not observe BRET signal saturation or the mode of binding deviated from a classical 1:1 stoichiometry, and thus, we were unable to obtain reliable BRET50 estimates. In these cases, differences in binding strength between wildtype and mutant constructs can be assessed using BRET measurements at fixed sub-saturation acceptor/donor transfection ratios under conditions where mutant and wildtype proteins expressed equally. Monitoring the expression levels of mutant constructs is important to rule out loss of binding because of a destabilization of the protein. However, we cannot exclude the possibility that some expressed mutants might still be partially unfolded or mislocalized and thus, some loss of binding detected in our study might be unspecific and not the result of a specific perturbation of the predicted interface. Furthermore, preservation of binding observed for some other mutants at the predicted interface might result from the mutations not being disruptive enough and thus, do not necessarily disprove the predicted interface. All mutations in this study were designed manually from inspection of the structural models. Mutation design could be improved in future studies using tools that predict the effect of mutations on protein folding or binding. In addition, using deletion constructs can be informative as seen for PEX16, but are also more likely to alter expression levels (i.e. for STX1B and FBXO28) or the distance of the donor and acceptor to each other and thus, make BRET comparisons more problematic.

Despite these limitations, we were able to assess the validity of seven interface predictions using experimentation. We discovered a likely novel DMI type that mediates binding between PEX3 and PEX16, and proposed a model for how PEX3, PEX16, and PEX19 form a trimeric complex at the peroxisomal membrane. We also validated a variation of the LIG_GYF motif class in SNRPB that mediates binding to GIGYF1 thereby potentially connecting mRNA splicing with posttranscriptional control mechanisms. These results confirm in principle that AF is able to predict novel interface types and that it can be used to extend existing interface type definitions. However, our experimental results also highlight clear limitations of AF predictions. Our data suggests that FBXO28 and STX1B as well as STX1B and VAMP2 interact via coiled-coil interfaces but likely at higher stoichiometries and different conformations than predicted. We confirmed the binding pocket in ESRRG but not the predicted interfaces in PSMC5 and we could not substantiate interface predictions for TRIM37 and PNKP. Highly confident interface predictions were obtained for seven additional PPIs that we unfortunately could not further explore experimentally because the PPIs either retested as negative in the BRET assay or because we could not obtain wildtype, full length clones. In summary, we provided experimental evidence and structural information for PPIs whose disruption is likely associated with neurodevelopmental disorders. This information can be explored in future studies aimed at delineating potential molecular mechanisms causing disease. Our study furthermore laid out clear limitations, perspectives, and future needs in AI-based structure prediction to bring us closer to a fully structurally annotated human protein interactome.

Acknowledgements

We thank all members of the Luck, Gibson, and Schueler-Furman labs as well as Julian König for helpful discussions and input. We thank Izabella Krystkowiak and Norman Davey for helping us access the SLiMSearch resource with an API. We thank Fridolin Kielisch for advice on statistical analysis as well as the media lab and protein production core facilities of IMB. Support from IMB's IT department and especially help from Christian Dietrich for local installations of AlphaFold is gratefully acknowledged. The GPU cluster on which part of the AlphaFold predictions were performed was funded by the Ministry of Science and Health (MWG), Rhineland Palatinate (funding ID: TB-Nr.:3658/19). We are very thankful for support from EMBL IT Services and the HPC resources for running AlphaFold predictions for this project. This work is funded by the Deutsche Forschungsgemeinschaft (DFG, German Research Foundation) – Project-ID LU 2568/1-1 awarded to K.L.. J.S. acknowledges a PhD stipend from IMB's collaborative research initiative. J.K.V. was supported by the European Union's Horizon 2020 UBIMOTIF programme (860517). This work was supported, in whole or in part, by the Israel Science Foundation, founded by the Israel Academy of Science and Humanities (grant number 301/2021 to O.S.-F.).

Author contributions

Chop Yan Lee: Project administration, data curation, formal analysis, investigation, methodology, visualization, writing - original draft, writing - review and editing. **Dalmira Hubrich:** Data curation, formal analysis, investigation, methodology, visualization, writing - original draft, writing - review and editing. **Julia K. Varga:** Data curation, formal analysis, investigation, visualization, writing - original draft, writing - review and editing. **Christian Schäfer:** Data curation, investigation, methodology. **Mareen Welzel:** Investigation. **Eric Schumbera:** Methodology. **Milena Đokić:** Data curation. **Joelle M. Strom:** Formal analysis, investigation, visualization. **Jonas Schönfeld:** Investigation. **Johanna L. Geist:** Investigation. **Feyza Polat:** Investigation. **Toby J. Gibson:** Provided resources, supervision, writing - review and editing. **Claudia Isabelle Keller Valsecchi:** Funding acquisition, supervision, investigation, writing - review and editing. **Manjeet Kumar:** Provided resources, methodology, formal analysis, writing - review and editing. **Ora Schueler-Furman:** Conceptualization, funding acquisition, supervision, writing - original draft, writing - review and editing. **Katja Luck:** Conceptualization, funding acquisition, project administration, supervision, data curation, formal analysis, investigation, methodology, visualization, writing - original draft, writing - review and editing. Author contributions are defined using the CRediT system as requested by the journal.

Conflict of interest

The authors declare that they have no conflict of interest.

Materials and Methods

Selection of structures for DMI benchmark dataset

To gather a list of ELM classes with structural evidence and annotate their minimal interacting fragments, we downloaded a dataset of solved structures of all ELM classes from ELM DB on 08.10.2021 (ELM class version 1.4) for instances that are annotated as true positives (Kumar *et al*, 2022). The structures were subject to a series of manual inspections to check their validity for further analysis. First, since AlphaFold can only model the 20 standard amino acids, we excluded any structures with post-translational modifications in the motif. Structures that do not solve all of the residues in a motif as curated by ELM DB were excluded. Third, we restrict our studies to only binary interactions, so DMIs that require more than two proteins to form the binding interface were excluded. Likewise, DMIs with only intramolecular interaction evidence were excluded. We manually annotated the boundaries of the domains by visual inspection of the structures. After this filtering, we identified 136 structures from 136 different ELM classes that formed our DMI benchmark dataset (Table S1).

Selection of structures for the DDI benchmark dataset

We randomly selected 100 pairs of Pfam domain types that were described in the 3did resource (Mosca *et al*, 2014) to be in contact with each other in solved structures in the Protein

Data Bank (PDB). We manually inspected all PDB entries listed to contain contacts between instances of a given Pfam domain pair until we found one that we considered a genuine domain-domain interaction. These decisions were primarily based on the number of atomic contacts observed and the validity that two folded domains were interacting with each other. Out of the 100 selected Pfam domain pairs, we identified 58 DDI types and 58 corresponding approved DDI structural instances that we selected for the DDI benchmark dataset. The sequences of the minimal interacting domain regions were manually annotated by visual inspection of the structures and used for prediction. A more detailed description of the curation procedure and information on the pairs will be soon published elsewhere (Geist et al in preparation).

Generation of random reference sets with minimal interacting regions

Mutating motif sequences

Key conserved residues of the motifs in the DMI benchmark dataset were identified computationally using the regular expression of the corresponding ELM class in the ELM DB and SLiMSearch (Krystkowiak & Davey, 2017). The defined positions are any positions in the regular expression that are not wildcards. To mutate the key residues to the ones with opposite physico-chemical properties, we substituted one or two key residues with the ones that are of the largest Miyata distance (Miyata *et al*, 1979) (Table S2).

Randomizing pairings of known domain motif interfaces

To simulate non-binding domain-motif pairs, we randomized the pairings of known domain motif interfaces. As some domain types can bind to motifs from distinct ELM classes, we manually checked that the randomized pairings did not coincide with actual domain-motif interface types (Table S2).

Randomizing pairings of known domain-domain interfaces

The pairings between known domain-domain interfaces were randomized to form the random reference set for DDIs (Table S2).

Generation of positive DMI reference set with fragment extensions

Among the 136 solved structures that we selected previously, we further filtered for structures that consist of only human proteins. To test the potential effect of extension on DMIs that were predicted with different accuracies in their minimal forms, we selected 12 DMI types from the correct sidechain category, 8 DMI types from the correct backbone category and 11 DMI types from the correct pocket category as determined using the motif RMSD calculation. In total, 31 DMI types were selected for extension. Three additional DMI types were originally selected but later on discarded because they contained secondary motif occurrences complicating data analysis. The extensions were done on the canonical sequence of the proteins used to solve the structure. Motif extension 1 extended the motif sequence at both N and C termini by n residues where *n* is the length of the known motif. Motif extension 2 further extended the motif sequence by another *n* residues at both termini. Motif extension 3 and 4 each extended the motif sequence by 2*n* residues at both termini. Motif extension 5 extended the motif sequence by including neighboring domains and motif extension 6 used the full-length protein sequence. On the domain side, domain extension 1 extended the domain sequence to include the disordered regions N- and C-terminal of the binding domain until its neighboring domain(s) boundaries. Domain extension 2 included the sequence region of the neighboring domains and domain extension 3 used the full-length protein sequence. In cases where the known motif or binding domain is at the C terminus, we extended the motif or domain sequence on only the N terminus and vice versa. There were some cases where the last extension steps, motif extension 6 and domain extension 3, extended the protein minimally (less than 20 residues N or C terminal to the previous extension step). These cases were excluded from the analysis. The dataset of extended DMIs is in Table S4. In total, 709 fragment pairs were submitted to AlphaFold. From these, 632 and 616 were successfully predicted by AF v2.2 and v2.3, respectively.

Generation of random DMI reference set with fragment extensions

To generate a random reference set using the extensions, we randomized the pairings of the 34 DMI types that we selected for extensions and paired their extensions for prediction. Motif extension 6 and domain extension 3 were excluded from the pairing. The dataset of DMIs with random pairings and their extensions can be found in Table S5. In total, 612 predictions were generated, among which 566 and 522 predictions were successfully predicted by AF v2.2 and v2.3, respectively. Since motif extension 6 and domain extension 3 were excluded from the random reference set using the extensions, we also excluded them from the positive reference set extensions during ROC analysis. This resulted in 563 and 540 predictions from the positive reference set extensions for AF v2.2 and v2.3, respectively.

Selection of reference datasets for comparison of AF v2.2 with v2.3

All predictions for the minimal DMIs and the random DMIs involving minimal fragments were successfully predicted by both versions of AF. Some extensions from the positive reference set were not successfully predicted by AF v2.2 and v2.3 due to failure from HHblits. To compare AF v2.2 with v2.3, we used only predictions that were successfully predicted by both versions of AF. This resulted in 616 predictions from the extensions of the positive reference set.

Selection of DMI structures and randomization to evaluate specificity of fragmentation approach

Among the 34 DMIs selected for extension, we further selected 20 DMIs and randomized their pairing to form random domain-motif protein pairs. These random protein pairs were subject to the fragmentation approach and generated 11045 fragment pairs of which 11044 resulted in an AlphaFold prediction. The information on random protein pairs, their prediction result and statistics were stored in Table S7.

AlphaFold versions and runs

We used a local installation of AlphaFold Multimer version 2.2.0 and 2.3.0 (Evans *et al*, 2021) for all protein complex predictions with the following parameters:

```
--max_template_date=2020-05-14
--db_preset=full_dbs
--use_gpu_relax=False
```

For every AlphaFold run, five models were predicted with single seed per model by setting the following parameter:

```
--num_multimer_predictions_per_model=1
```

The databases queried during AlphaFold predictions were specified following the instructions from the github page of AlphaFold (https://github.com/deepmind/alphafold#running-alphafold):

For running AlphaFold Multimer v2.2, the following databases were queried:

```
--bfd_database_path=bfd_metaclust_clu_complete_id30_c90_final_seq.sorted_opt
--mgnify_database_path=alphafold_v220_databases/mgy_clusters_2018_12.fa
--obsolete_pdbs_path=alphafold_v220_databases/pdb_mmcif/obsolete.dat
--pdb_seqres_database_path=alphafold_v220_databases/pdb_seqres/pdb_seqres.txt
--template_mmcif_dir=alphafold_v220_databases/pdb_mmcif/mmcif_files
--uniprot_database_path=alphafold_v220_databases/uniprot/uniprot.fasta
--uniclust30_database_path=alphafold_v220_databases/uniclust30/uniclust30_2018_08/uniclust30_2018_08
--uniref90_database_path=alphafold_v220_databases/uniref90/uniref90.fasta
```

For running AlphaFold Multimer v2.3, the following databases were queried:

```
--bfd_database_path=alphafold_v230_databases/bfd/bfd_metaclust_clu_complete_id30_c90_final_seq.sorted_opt
--mgnify_database_path=alphafold_v230_databases/mgnify/mgy_clusters_2022_05.fa
--obsolete_pdbs_path=alphafold_v230_databases/pdb_mmcif/obsolete.dat
--pdb_seqres_database_path=alphafold_v230_databases/pdb_seqres/pdb_seqres.txt
--template_mmcif_dir=alphafold_v230_databases/pdb_mmcif/mmcif_files
--uniprot_database_path=alphafold_v230_databases/uniprot/uniprot.fasta
--uniref30_database_path=alphafold_v230_databases/uniref30/UniRef30_2021_03
--uniref90_database_path=alphafold_v230_databases/uniref90/uniref90.fasta
```

To test the effect of template use on prediction accuracy, the following parameter setting was used to switch off the use of templates during the prediction:

```
--max_template_date=1950-01-01
```

For the fragmentation approach, the multiple sequence alignments (MSAs) of a given protein fragment can be reused in subsequent runs where the same fragment is involved. The MSAs were first moved to the prediction output folder and the following parameter was added to enable the reuse of MSAs.

```
--use_precomputed_msas=True
```

For efficient computing, we segregated the MSA generation part by using only the CPUs and the model fitting part using the GPUs.

Calculation of metrics for structural models

Motif RMSD

We used the software PyMOL (TM) Molecular Graphics System, Version 2.5.0. Copyright (c) Schrodinger, LLC., for the superimposition of AlphaFold models with corresponding solved structures. First, we used the align command to align the domain chain in AlphaFold models with the domain chain in the solved structure. Then, we used the rms_cur command to calculate the all-atom RMSD between the motif chain in AlphaFold models and the motif chain in the solved structure. To ensure that the RMSD calculation was done based on all atom identifiers and without any outlier rejection refinement, the arguments of the rms_cur command, matchmaker and cycles, were set to 0.

DockQ

The calculation of DockQ scores of AlphaFold models was done in reference to their solved structures using the code available on the github repository of DockQ (https://github.com/bjornwallner/DockQ, (Basu & Wallner, 2016).

pDockQ

The calculation of pDockQ of AlphaFold models was done by adapting the code available on the github repository from the Elofsson lab (https://gitlab.com/ElofssonLab/FoldDock/-/blob/main/src/pdockq.py, (Bryant *et al*, 2022)). The pDockQ score is created by fitting a sigmoidal curve to the DockQ scores of a series of AlphaFold predicted models. The score takes into account the number of interface contacts as well as their pLDDT scores. Of note, the calculation of pDockQ score takes Cβs (Cα for glycine) from different chains within 8 Å from each other as interface contacts which is different from our interface definition (see the subsection below *Domain chain and motif chain interface pLDDT and average interface pLDDT)*.

iPAE

The calculation of iPAE of AlphaFold models was done by adapting code available on the github repository https://github.com/fteufel/alphafold-peptide-receptors/tree/main (Teufel *et al*, 2023). The iPAE is the median predicted aligned error at the interface. The authors consider residues in contact if their distance is below 0.35nm (3.5Å). The iPAE score could not be calculated for models generated by AlphaFold Multimer version 2.3.0 due to JAX dependency of the pickle files generated by AlphaFold Multimer version 2.3.0.

Model confidence

The model confidence of AlphaFold models was extracted from the ranking_debug json file. The model confidence is a weighted combination of pTM and ipTM to account for both intra- and interchain confidence:

$$model\ confidence = 0.8 \cdot ipTM + 0.2 \cdot pTM$$

Domain chain and motif chain interface pLDDT and average interface pLDDT

Since AlphaFold conveniently stores the pLDDT confidence measure for each residue in the B-factor field of the output PDB files, the pLDDT of residues at the interface was parsed from the output PDB files of AlphaFold. Residues at the interface are defined as those that have at least one heavy atom that is less than 5Å away from any heavy atom of the other chain (calculated using the PyMOL API). The pLDDT of the residues at the interface from the domain chain and motif chain was averaged to compute the domain chain and motif chain interface pLDDT, respectively. The pLDDT of all the residues from both chains was averaged to compute the average interface pLDDT.

Residue-residue and atom-atom contacts

Following the interface definition above, the number of unique residue-residue and atom-atom contacts were also quantified as measurements to assess AlphaFold models.

Quantification of motif properties

Motif hydropathy score and symmetry score

By referring to the Kyte-Doolittle hydrophobicity scale, (Kyte & Doolittle, 1982) the hydropathy scores of the amino acids in a given motif were summed and averaged to compute the average hydropathy of the motif. The average motif symmetry score was computed by taking the sum of the absolute difference of hydropathy scores between motif position n and n - motif length + 1 and division of this sum by half of the motif length:

$$Peptide\ symmetry\ score = \frac{\sum_{n=1}^{a} |(H_n - H_{x-n+1})|}{a}$$

where x is the length of the motif and a is the floor division of x by 2.

Motif probability

The motif probability reflects the degeneracy of a given motif class as quantified by its regular expression that is annotated in the ELM DB. The motif probability was retrieved from the ELM DB version 1.4.

Secondary structure elements of motifs

We extracted the secondary structure elements of motifs using the PyMOL API. In cases where the motif adopts partial secondary structure, such as loop-helix-loop or loop-strand-loop, they are treated as helical or strand, respectively.

Selection of motif classes from ELM DB without annotated structural instances and prediction with AlphaFold

By querying the ELM DB for all ELM classes, we retrieved a list of ELM classes and the number of instances with a structure solved (column #instances_in_PDB). We filtered for ELM classes with 0 instances_in_PDB and selected 205 instances out of the filtered ELM classes for AF prediction. The ELM instances were extended at both N and C termini by n residues where *n* is the length of the ELM instance, according to the benchmarking results. The minimal binding domains of the ELM instances were detected in the interaction partner using Pfam HMMs (Mistry *et al*, 2021). As the domain boundaries detected by Pfam HMMs could be inaccurate, we also extended the domain sequence at the N and C terminus by 20 residues to ensure that the whole folded region was covered. The predictions were performed using AF version 2.3.0. To select a subset of these motif classes, where we can do experimental testing, we also used the InParanoid resource (Persson & Sonnhammer, 2023) to map ELM instances where both proteins are from mouse to their human orthologs. To verify that they indeed do not have structural homologues in the PDB, we both used the SIFTS mapping (Dana *et al*, 2019) between the Pfam domain in ELM and the PDB and also looked at the ELM classes that were listed as homologs on the ELM website.

Evaluation of effect of fragment extensions on AF prediction accuracies

We superimposed the AF models generated with DMI extensions onto the corresponding solved DMI structures to quantify AF prediction accuracy using motif RMSD calculations. To this end, we aligned the two structures on their minimal binding domains and calculated the all-atom RMSD between the minimal motif in the extension AF model and the minimal motif in the solved structure. To determine potential differences in DMI prediction accuracy when using minimal versus extended protein fragments, we computed the log2 fold change of the all-atom motif RMSD before and after extension.

$$Fold\ change\ in\ prediction\ accuracy\ = log_2(\frac{all\ atom\ RMSD\ motif_{minimal\ DMI}}{all\ atom\ RMSD\ motif_{extended\ DMI}})$$

Fragment design and fragment pairing for fragmentation approach

We first inspected the monomeric structural models from the AlphaFold database (Varadi *et al*, 2022) of both interacting proteins to determine the boundaries of their ordered and coiled-coil regions, which were also treated as “ordered”. All regions that were not annotated as ordered were annotated as disordered. In some cases, an extended loop with low pLDDT can be found within an ordered region. As they can also potentially carry a motif or mediate interactions in another way, these regions were also annotated as disordered in addition to their annotation as being part of a larger ordered region. The disordered regions of the proteins were fragmented into fragment sizes of 10, 20 and 30 residues. To allow AF to sample continuous sequences, we also generated another set of fragments of same sizes that overlap with the previous fragments by sliding the sequence by half the size of the fragment. The unfragmented disordered regions, as well as their fragments, from one protein were then paired with the ordered regions from its interacting partner and vice versa for prediction. The ordered regions from both proteins were also paired for prediction.

Selection of NDD proteins

A list of NDD genes was assembled using whole exome and whole genome sequencing studies of cohorts of NDD patients from Gene4Denovo (Zhao *et al*, 2020) and Deciphering Developmental Disorders (DDD) study (Firth *et al*, 2011), respectively. From Gene4Denovo, we selected genes linked to autism-spectrum disorders (ASD), intellectual disability (ID), epilepsy (EE), undiagnosed developmental disorders (UDD) and NDDs in general. Genes with non-coding mutations as well as genes with a false discovery rate (FDR) >= 0.05 were excluded. Similarly, in the DDD study, genes associated with developmental disorders with a neurological component, as well as genes found to be mutated in at least three children with NDDs (labeled as confirmed genes) were retained. The final list included 984 NDD-risk genes. We filtered the HuRI network (Luck *et al*, 2020) for interactions mediated exclusively by proteins from this NDD gene list. Self-interactions were excluded. Since our fragmentation approach generates many fragments, we did not consider PPIs involving proteins that are more than 1500 amino acids in length.

Manual inspection of interface predictions for NDD-NDD PPIs

Paired fragments from NDD-NDD PPIs were predicted using AF version 2.2 and the prediction results are stored in Table S8. We manually inspected all NDD-NDD PPIs that obtained at least one structural model with either an average motif interface pLDDT of ≥ 70 for the disordered fragment or with a model confidence of ≥ 0.7 for ordered-ordered fragment pair interface predictions. We inspected the ranked_0 models for all fragment pairs that met the above cutoffs. For every NDD-NDD PPI we used Interactome3D (Mosca *et al*, 2013) and PDB database searches (https://www.rcsb.org/ (Berman *et al*, 2000)) to identify whether a structure already existed for this PPI. In our evaluation of the structural models we also considered if a certain interface was recurrently predicted for different overlapping fragments because this usually hints at increased confidences for the correctness of the interface prediction. We furthermore explored the number and kind of residue-residue contacts predicted by AF by visual inspection of the structural models using PyMol. We searched for functional annotations and existing structures for the monomers using the PDB, ProViz (Jehl *et al*, 2016) , SMART (Letunic *et al*, 2021), and the scientific literature to identify enzymatic pockets or binding interfaces for DNA, RNA, or metal ions. Observations and justifications for the final evaluation of the predictions for every NDD-NDD PPI are provided in Text S1.

Softwares used

We used the software PyMOL (TM) Molecular Graphics System, Version 2.5.0. Copyright (c) Schrodinger, LLC., for the visualization and superimposition of AlphaFold models.

All codes were written in Python3 and analyses were done using Jupyter notebooks. We used the Python libraries pandas (McKinney, 2010) for data analysis, and Matplotlib (Hunter, 2007) and seaborn (Waskom, 2021) for data visualization. ROC and PR statistics were calculated using the Python package sci-kit learn (Pedregosa *et al*, 2012).

Cell line culture and maintenance

HEK293 cells were grown and maintained in DMEM (Thermo Fisher), supplemented with 10% FBS (PAN-Biotech), 2 mM glutamine (Thermo Fisher) and 1% penicillin–streptomycin (Thermo Fisher). Cells were incubated at 37°C with 5% CO_2 . Subcultivation was performed with 1 ml of 0.05% trypsin every 2–3 days for up to 40 passages. For each passage 1-2x10^6 cells were seeded in T25 flasks (Sarstedt). Then, new cells were thawed from stocks containing 2×10^6 cells in 1 ml of growth medium, supplemented with 10% DMSO (Sigma). Every 3 months cells were checked for mycoplasma contamination using a PCR test (Table S9).

Plasmid construction

Standard controls

The donor and acceptor vectors pcDNA3.1-cmyc-NL-GW (Addgene plasmid ID #113446), pcDNA3.1-GW-NL-cmyc (Addgene plasmid ID #113447), pcDNA3.1 GW-His3C-mCit, pcDNA3.1 mCit-His3C-GW as well as controls pcDNA3.1-NL-cmyc (Addgene plasmid ID #113442), pcDNA3.1-PA-mCit (Addgene plasmid ID #113443) were kindly provided by the Wanker Group (Max-Delbrück-Centrum für Molekulare Medizin, Germany) (Table S10). By default we cloned all ORFs of interest into N-terminal NL and mCit fusion destination vectors and occasionally also transferred ORFs into C-terminal fusion vectors if N-terminal fusions did not result in sufficient BRET signals but the interaction was of high interest to this study and predicted interfaces were closer to the C-terminus (Table S11). Trepte et al have shown that testing protein pairs in different configurations increases detection rates while maintaining low false detection rates and that BRET signals are higher if fusions are close to the actual interaction interface (Trepte *et al*, 2018; preprint:Trepte *et al*, 2021; preprint:Trepte *et al*, 2023).

GATEWAY cloning procedure

Full-length wild-type human open reading frames (ORFs) being cloned in GATEWAY entry vectors from the ORFeome collaboration are stored as bacterial glycerol stocks. (ORFeome Collaboration, 2016)

1. The ORFs were inoculated in 96-well plates (Corning), with each well containing 200 uL of LB medium and 100 µg/ml ampicillin. The plate was incubated at 37°C and left to shake overnight at 190 rpm.
2. In a 96-well PCR plate (Brand) 10 ng of each selected ORF was used per 50 µl PCR reaction (denaturation at 98°C for 10 s, annealing at 55°C for 30 s and extension at 72°C for 3 min, 30 cycles of amplification) using phusion high-fidelity polymerase (NEB) and primers annealing to the backbone of the plasmid (forward: 5'TTGTAAAACGACGGCCAGTC and reverse: 5' GCCAGGAAACAGCTATGACC).
3. The PCR products (6 µl per well) were confirmed through 96-well E-gel with SYBR (Thermo Fisher, Catalog no G720801) using 25 µl of loading buffer (Thermo Fisher) and 20µl of E-Gel 96 High range DNA marker (Thermo Fisher).
4. In a 96-well PCR plate 1 µl of each amplified PCR product together with 200 ng of above-mentioned destination vectors were directly used per 10 µl LR reaction using 4x LR clonase (Invitrogen), thereby generating expression vectors.
5. The full 10 µl of LR reaction was transformed into chemically competent DH5a cells (30 µl) in a 96-well PCR plate, then recovered in 80 µl of pre-warmed SOC medium at 37˚C for 1 hour without shaking.
6. 70 µl of transformed bacteria was plated on 48-well square agar plates and incubated at 37°C overnight.
7. Afterwards, colonies were selected and inoculated into a 96 deep-well plate containing 2 ml of LB medium and 100 µg/ml ampicillin. The plate was then incubated at 37˚C with continuous shaking at 700 rpm in the incumixer for 24 hours.
8. The amplified vectors were extracted from the inoculated culture using Plasmid Plus 96-well Miniprep kit (Qiagen). The concentration of each vector was measured with a Nanophotometer and diluted to 100 ng/µl. Next, 600 ng of insert was used for full-length sequencing using the backbone primers (tag-specific NanoLuc forward: 5'GAACGGCAACAAAATTATCGAC, mCitrine forward: 5'AGCAGAATACGCCCATCG and reverse: 5'GGCAACTAGAAGGCACAGTC) and ORF-specific primers (Table S9) to fully cover the ORFs where it was needed (Table S10).

Site-directed mutagenesis

The primers were manually designed using the following criteria:

1. For point mutation the primers should overlap the site of mutation. The overlap should be 15-20 nucleotides (nt).
2. For the deletion the primers should be designed to exclude the deletion site, but still overlap and the overlap should be as mentioned in step 1.
3. Primer length should be in the range of 32-36 nt.
4. GC content should be between 40-60%.
5. Difference in melting temperature of primers should not exceed 5°C.
6. The primer ideally should start and end with guanine or cytosine.

7. The designed oligos were grouped by annealing temperature for the next step.
8. In 96-well PCR plate 10 ng of DNA template together with oligos were used per 50 uL of PCR reaction (denaturation at at 98°C for 2 min, annealing for 15 s and extension at 72°C for 5 min, 25 cycles of amplification) using phusion high-fidelity polymerase (NEB).
9. 1 µL of DpnI (NEB) was added to the plate with PCR products and incubated at 37°C for 1 hour. The reaction was stopped at 65°C for 20 min.
10. The PCR products (6 µl per well) were confirmed through 96-well E-gel with SYBR (Thermo Fisher, Catalog no G720801) using 25 µl of loading buffer (Thermo Fisher) and 20µl of E-Gel 96 High range DNA marker (Thermo Fisher).
11. 3 µL of digested PCR product was transformed into chemically competent DH5a cells (30 µL) in a 96-well PCR plate, then recovered in 80 µL of pre-warmed SOC medium at 37˚C for 1 hour without shaking.
12. 70 µL of transformed bacteria was plated on 48-well square agar plates and incubated at 37°C overnight.
13. Afterwards, colonies were selected and inoculated into a 96 deep-well plate containing 2 ml of LB medium and 100 µg/ml ampicillin. The plate was then incubated at 37˚C with continuous shaking at 700 rpm in the incumixer for 24 hours.
14. The amplified vectors were extracted from the inoculated culture with Plasmid Plus 96-well Miniprep kit (Qiagen). The concentration was measured with a Nanophotometer and diluted to 100 ng/µl. Next, 600 ng of insert was used for full-length sequencing using primers covering the mutation and ORF-specific primers (Table S9) to fully cover the ORF length (Table S10).

BRET assay

Transfection

HEK293 cells were grown and maintained in high-glucose (4.5 g/l) DMEM (Thermo Fisher) for BRET assays. Media was supplemented with 10% fetal bovine serum (PAN-Biotech) and 1% Penicillin/Streptomycin. Cells were grown at 37 °C, 5% CO_2, and 85% RH. Cells were subcultured every 2-3 days and transfected with lipofectamine 2000 transfection reagent (Invitrogen) in Opti-MEM medium (Thermo Fisher) using the reverse transfection method according to the manufacturer's instructions. For transfections, cells were seeded at a density of 4.0 x 10^4 cells per well in a white 96-well microtiter plate (Greiner) in phenol-red-free, high-glucose DMEM media (Thermo Fisher) supplemented with 5% fetal bovine serum (Thermo Fisher). Transfections were performed with a total DNA amount of 200 ng per well. If the expression plasmid concentration amount was below 200 ng/well, pcDNA3.1 (+) was used as a carrier DNA to reach the total amount of DNA of 200 ng. All protein pairs were tested in both N-terminal fusion orientations (NL-A with mCit-B and NL-B with mCit-A). The following proteins were also tested as C-terminal fusions: CSNK2B-NL, ESRRG-NL, CUL3-NL, PEX3-NL, PEX19-NL, PSMC5-NL, PEX3-mCit, PEX19-mCit, PEX16-mCit, RORB-mCit, ESRRG-mCit, PAX6-mCit, CSNK2B-mCit, PSMC5-mCit, KCTD7-mCit (Table S10).

Measurement

The plate was incubated 2 days at 37 °C, 5% CO_2, and 85% RH before measurements. All measurements were done with the Infinite M200 Pro microplate reader (Tecan). First, 100 µl of the medium was aspirated from each well. The mCitrine fluorescence (FL) was measured in intact cells (excitation/emission 513 nm/548 nm) using a gain of 100. On rare occasions, the plate reader recorded an overflow with these settings (i.e. for GIGYF1 constructs). In these cases, we repeated the measurement with optimal gain settings and used a fluorescein control to normalize fluorescence signals measured with different gain settings. For this purpose, Fluorescein was obtained from Sigma-Aldrich (Catalog No 46955-250MG-F) and used without further purification. A stock solution of Fluorescein (1mg/ml in Ethanol) was prepared by dissolving 1.3 mg Fluorescein in 1.3 ml absolute ethanol. 100 µl of a 20 µg/ml solution of Fluorescein were added to an empty well immediately before starting the fluorescence measurements. The 20 µg/ml solution of Fluorescein was obtained by preparing a 1:50 dilution in water of the stock solution. After measuring the fluorescence, coelenterazine-h (PJK Biotech GmbH) was added to a final concentration of 5 µM. The cells were briefly shaken for 15 s and incubated for 15 min inside the plate reader at 37 °C. After incubation, total luminescence was measured first followed by short-wavelength (WL) and long-wavelength luminescence (LU) measurements using the BLUE1 (370-480 nm) and the GREEN1 (520-570 nm) filters at 1,000 ms integration time. Corrected BRET ratios were calculated as described in (Trepte *et al*, 2018). Briefly, for every transfected protein pair NL-A and mCit-B, the following two control pairs were measured: NL-Stop with mCit-B and NL-A with mCit-Stop. The maximal BRET from both control pairs was subtracted from the actual test pair to correct for donor bleedthrough, unspecific binding to the tags, and background signal.

Determination of binding events in BRET assay

To determine whether a protein pair interacted in the BRET assay or not, we used donor:acceptor DNA transfection ratios of 2:50 ng in all cases except for PEX3-PEX16 where we used 8:25 and PEX3:PEX19 where we used 8:50 ng DNA ratios due to low expression levels of PEX3 and a degradation effect of higher PEX16 protein levels on PEX3 expression levels. We requested that cBRETs determined at these transfection ratios were ≥ 0.05, fluorescence measurements representing mCitrine fusion expression levels to be ≥ 500 units, and total luminescence measurements representing NL fusion expression levels to be ≥ 50000.

Saturation Assay

For donor saturation experiments various donor DNA amounts (1, 2, 4 and 8 ng) encoding NL-fused proteins were co-transfected with increasing amounts of acceptor DNA (12.5, 25, 50, 100, 200 ng) encoding mCitrine-fused proteins. Fluorescence, total luminescence, and BRET measurements were done as described before. BRET measurements were corrected for bleedthrough using NL-Stop transfections. Fluorescence and total luminescence measurements were corrected for background signal using transfections with pcDNA3.1(+) and subsequently used to estimate amounts of expressed proteins and to plot acceptor/donor ratios on the x-axis of titration plots.

Fitting of titration curves

Titration curves were fitted using the leastsq function from the scipy.optimize python package (Virtanen *et al*, 2020) using the model BRET = ((A/D) * BRETmax)/(BRET50 + (A/D)) described in (Drinovec *et al*, 2012) to obtain estimates for the BRETmax and BRET50. Standard errors of the BRET50 estimates were obtained from the variance-covariance matrix, calculated by multiplying the fractional covariance matrix (output by leastsq function) by the residual variance. Measuring BRET signals in intact cells for increasing acceptor/donor protein expression ratios results in an eventual saturation of the signal. Fitting this curve allows extraction of the maximal BRET that can be reached and the BRET50, which is the acceptor/donor ratio at which half of the maximal BRET is obtained. The BRET50 is indicative of binding affinity, in analogy to the IC50, however, its accurate estimation requires saturation of the BRET to be observed in the experimental system, which cannot always be achieved because of limited amounts of DNA that cells can be transfected with. Alternatively, if mutations are unlikely to change the overall structure of the fusion constructs and do not alter expression levels compared to wildtype, single point BRET measurements at acceptor/donor ratios prior to BRET saturation are also indicative of changes in binding strength.

Antibodies

Purified anti-HA.11 Epitope Tag, Clone: [16B12], Mouse, Monoclonal (Biolegend, BLD-901502), 1:2000.
Purified anti-GIGYF1, Rabbit, Polyclonal (BETHYL laboratories, Cat. #A304-132A-1), 1:1000.
GAPDH Loading Control Monoclonal Antibody (GA1R), HRP-coupled (Thermo Fisher Cat. MA515738HRP), 1:3000.

Co-immunoprecipitation and western blot

Snrpb (full-length) and C-terminal truncation mutant (amino acids 1-190) was cloned from mouse cDNA and ligated into pFRT-TO destination plasmid using AscI and PacI restriction sites. The constructs additionally contain C-terminal 2xHA and mNeonGreen tags. Flp-In™ T-REx™ 293 Cell Lines (Thermo Fisher, catalog number: R78007) expressing Snrpb endogenously from a single locus were generated according to the manufacturer's instructions. In brief, pFRT-TO and pOG44 plasmids were co-transfected and hygromycin-resistant colonies were grown, picked and expanded. The Snrpb transgene expression was validated by Western blot, RT-qPCR, and immunofluorescence, which showed that ectopic Snrpb-HA was expressed at levels highly similar to the endogenous Snrpb protein (data not shown).
For the co-immunoprecipitation experiments, 8x106 cells were seeded in a 10 cm dish. The following day, expression of Snrpb-HA was induced by adding 0.1 µg/mL Doxycycline (D9891, Sigma Aldrich) to the culture medium. Parental cells not expressing any HA-tagged transgene were used as a negative control of immunoprecipitation. The next morning the cells were harvested by scraping in culture media, followed by centrifugation and a single wash in ice-cold PBS. The whole cell extract was prepared by 15 min incubation on ice with 0.3 mL of lysis buffer (200 mM NaCl, 50 mM HEPES, pH 7.6, 0.1% IGEPAL, 10 mM MgCl2, 10% Glycerol, Protease Inhibitor Cocktail (P8340, Sigma Aldrich), Phosphatase Inhibitor (P5726, Sigma Aldrich) followed by 2 cycles of sonication in a Bioruptor Plus (30 seconds on, 30 seconds off) and centrifugation for 20 minutes at 16000xg. The extract was quantified by a Bradford assay and 1 mg was used for immunoprecipitation, for which the NaCl concentration was adjusted to 100 mM final concentration by diluting with an equal volume of Lysis Buffer containing 0 mM NaCl. 0.05 mg was set aside as input control (5%). 0.02 mL of Thermo Scientific™ Pierce™ Anti-HA Magnetic Beads (Thermo Fisher Cat. 13464229) were incubated with 1 mg protein extract for 1 hour at 4°C on a rotating wheel. The beads were washed 3 times before eluting the immunoprecipitated proteins with 0.02 mL of 1 x NuPAGE™ LDS Sample Buffer by incubating at 42°C for 10 min while shaking at 800 rpm. Another 0.01 mL were used for elution, were then combined making a total of 30 µL, which were transferred to a fresh tube and to which 3 µL of 1M DTT were added. Input and immunoprecipitated eluates were then separated on a 10% Tris-Glycine SDS PAGE using 1xMOPS buffer, immunoblotted on 0.45

μm PVDF membranes (Tris-Glycin Transfer Buffer, 10% Methanol, 300 mA, 1 hour), blocked with 5% milk in TBS-0.2% Tween for 30 min at RT. Primary antibodies were incubated overnight at 4°C on a rocker followed by washes and incubation with secondary HRP-labelled antibodies (1 hour at RT in 5% milk, TBS-0.2% Tween). Blots were developed using Pierce™ ECL Western Blotting Substrate (Thermo Fisher Cat. 32209) or SuperSignal West Femto Maximum Sensitivity Substrate Kit (Thermo Fisher Cat. 34095) and imaged on a ChemiDoc MP V3 (Biorad).

References

Aceytuno RD, Piett CG, Havali-Shahriari Z, Edwards RA, Rey M, Ye R, Javed F, Fang S, Mani R, Weinfeld M, et al (2017) Structural and functional characterization of the PNKP-XRCC4-LigIV DNA repair complex. Nucleic Acids Res 45: 6238–6251

Ajuh P, Chusainow J, Ryder U & Lamond AI (2002) A novel function for human factor C1 (HCF-1), a host protein required for herpes simplex virus infection, in pre-mRNA splicing. EMBO J 21: 6590–6602

Akdel M, Pires DEV, Pardo EP, Jänes J, Zalevsky AO, Mészáros B, Bryant P, Good LL, Laskowski RA, Pozzati G, et al (2022) A structural biology community assessment of AlphaFold2 applications. Nat Struct Mol Biol 29: 1056–1067

Basu S & Wallner B (2016) DockQ: A Quality Measure for Protein-Protein Docking Models. PLoS ONE 11: e0161879

Berman HM, Westbrook J, Feng Z, Gilliland G, Bhat TN, Weissig H, Shindyalov IN & Bourne PE (2000) The protein data bank. Nucleic Acids Res 28: 235–242

Bhatnagar S, Gazin C, Chamberlain L, Ou J, Zhu X, Tushir JS, Virbasius C-M, Lin L, Zhu LJ, Wajapeyee N, et al (2014) TRIM37 is a new histone H2A ubiquitin ligase and breast cancer oncoprotein. Nature 516: 116–120

Braun P, Tasan M, Dreze M, Barrios-Rodiles M, Lemmens I, Yu H, Sahalie JM, Murray RR, Roncari L, de Smet A-S, et al (2009) An experimentally derived confidence score for binary protein-protein interactions. Nat Methods 6: 91–97

Bret H, Andreani J & Guerois R (2023) From interaction networks to interfaces: Scanning intrinsically disordered regions using AlphaFold2. bioRxiv DOI:10.1101/2023.05.25.542287 [PREPRINT]

Bronkhorst AW, Lee CY, Möckel MM, Ruegenberg S, de Jesus Domingues AM, Sadouki S, Sumiyoshi T, Siomi MC, Stelzl L, Luck K, et al (2023) An extended Tudor domain within Vreteno interconnects Gtsf1L and Ago3 for piRNA biogenesis in Bombyx mori. bioRxiv DOI:10.1101/2023.03.23.533951 [PREPRINT]

Bryant P, Pozzati G & Elofsson A (2022) Improved prediction of protein-protein interactions using AlphaFold2. Nat Commun 13: 1265

Buel GR & Walters KJ (2022) Can AlphaFold2 predict the impact of missense mutations on structure? Nat Struct Mol Biol 29: 1–2

Bugge K, Brakti I, Fernandes CB, Dreier JE, Lundsgaard JE, Olsen JG, Skriver K & Kragelund BB (2020) Interactions by Disorder - A Matter of Context. Front Mol Biosci 7: 110

Burke DF, Bryant P, Barrio-Hernandez I, Memon D, Pozzati G, Shenoy A, Zhu W, Dunham AS, Albanese P, Keller A, et al (2023) Towards a structurally resolved human protein interaction network. Nat Struct Mol Biol 30: 216–225

Chang L & Perez A (2023) Ranking Peptide Binders by Affinity with AlphaFold. Angew Chem Int Ed 62: e202213362

Choi SG, Olivet J, Cassonnet P, Vidalain P-O, Luck K, Lambourne L, Spirohn K, Lemmens I, Dos Santos M, Demeret C, et al (2019) Maximizing binary interactome mapping with a minimal number of assays. Nat Commun 10: 3907

Dana JM, Gutmanas A, Tyagi N, Qi G, O'Donovan C, Martin M & Velankar S (2019) SIFTS: updated Structure Integration with Function, Taxonomy and Sequences resource allows 40-fold increase in coverage of structure-based annotations for proteins. Nucleic Acids Res 47: D482–D489

Davey NE, Van Roey K, Weatheritt RJ, Toedt G, Uyar B, Altenberg B, Budd A, Diella F, Dinkel H & Gibson TJ (2012) Attributes of short linear motifs. Mol Biosyst 8: 268–281

Drew K, Lee C, Huizar RL, Tu F, Borgeson B, McWhite CD, Ma Y, Wallingford JB & Marcotte EM (2017) Integration of over 9,000 mass spectrometry experiments builds a global map of human protein complexes. Mol Syst Biol 13: 932

Drinovec L, Kubale V, Nøhr Larsen J & Vrecl M (2012) Mathematical models for quantitative assessment of bioluminescence resonance energy transfer: application to seven transmembrane receptors oligomerization. Front Endocrinol (Lausanne) 3: 104

Durocher D, Taylor IA, Sarbassova D, Haire LF, Westcott SL, Jackson SP, Smerdon SJ & Yaffe MB (2000) The molecular basis of FHA domain:phosphopeptide binding specificity and implications for phospho-dependent signaling mechanisms. Mol Cell 6: 1169–1182

Ebersberger S, Hipp C, Mulorz MM, Buchbender A, Hubrich D, Kang H-S, Martínez-Lumbreras S, Kristofori P, Sutandy FXR, Llacsahuanga Allcca L, et al (2023) FUBP1 is a general splicing factor facilitating 3' splice site recognition and splicing of long introns. Molecular cell

Ernst JA & Brunger AT (2003) High resolution structure, stability, and synaptotagmin binding of a truncated neuronal SNARE complex. J Biol Chem 278: 8630–8636

Evans R, O'Neill M, Pritzel A, Antropova N, Senior AW, Green T, Žídek A, Bates R, Blackwell S, Yim J, et al (2021) Protein complex prediction with AlphaFold-Multimer. bioRxiv DOI:10.1101/2021.10.04.463034 [PREPRINT]

Ferry C, Gianni M, Lalevée S, Bruck N, Plassat J-L, Raska I, Garattini E & Rochette-Egly C (2009) SUG-1 plays proteolytic and non-proteolytic roles in the control of retinoic acid target genes via its interaction with SRC-3. J Biol Chem 284: 8127–8135

Firth HV, Wright CF & DDD Study (2011) The Deciphering Developmental Disorders (DDD) study. Dev Med Child Neurol 53: 702–703

Freiman RN & Herr W (1997) Viral mimicry: common mode of association with HCF by VP16 and the cellular protein LZIP. Genes Dev 11: 3122–3127

Freund C, Kühne R, Yang H, Park S, Reinherz EL & Wagner G (2002) Dynamic interaction of CD2 with the GYF and the SH3 domain of compartmentalized effector molecules. EMBO J 21: 5985–5995

Fujiki Y, Matsuzono Y, Matsuzaki T & Fransen M (2006) Import of peroxisomal membrane proteins: the interplay of Pex3p- and Pex19p-mediated interactions. Biochim Biophys Acta 1763: 1639–1646

Fujiki Y, Okumoto K, Honsho M & Abe Y (2022) Molecular insights into peroxisome homeostasis and peroxisome biogenesis disorders. Biochim Biophys Acta Mol Cell Res 1869: 119330

Henrie A, Hemphill SE, Ruiz-Schultz N, Cushman B, DiStefano MT, Azzariti D, Harrison SM, Rehm HL & Eilbeck K (2018) ClinVar Miner: Demonstrating utility of a Web-based tool *for viewing and filtering ClinVar data. Hum Mutat 39: 1051–1060*

Hunter JD (2007) Matplotlib: A 2D Graphics Environment. Comput Sci Eng 9: 90–95

Huttlin EL, Bruckner RJ, Navarrete-Perea J, Cannon JR, Baltier K, Gebreab F, Gygi MP, Thornock A, Zarraga G, Tam S, et al (2021) Dual proteome-scale networks reveal cell-specific remodeling of the human interactome. Cell 184: 3022-3040.e28

Islinger M, Voelkl A, Fahimi HD & Schrader M (2018) The peroxisome: an update on mysteries 2.0. Histochem Cell Biol 150: 443–471

Jehl P, Manguy J, Shields DC, Higgins DG & Davey NE (2016) ProViz-a web-based visualization tool to investigate the functional and evolutionary features of protein sequences. Nucleic Acids Res 44: W11-5

Jilani A, Ramotar D, Slack C, Ong C, Yang XM, Scherer SW & Lasko DD (1999) Molecular cloning of the human gene, PNKP, encoding a polynucleotide kinase 3'-phosphatase and evidence for its role in repair of DNA strand breaks caused by oxidative damage. J Biol Chem 274: 24176–24186

Johansson-Åkhe I, Mirabello C & Wallner B (2021) Interpeprank: assessment of docked peptide conformations by a deep graph network. Front Bioinform 1: 763102

Jumper J, Evans R, Pritzel A, Green T, Figurnov M, Ronneberger O, Tunyasuvunakool K, Bates R, Žídek A, Potapenko A, et al (2021) Highly accurate protein structure prediction with AlphaFold. Nature 596: 583–589

Kallijärvi J, Lahtinen U, Hämäläinen R, Lipsanen-Nyman M, Palvimo JJ & Lehesjoki A-E (2005) TRIM37 defective in mulibrey nanism is a novel RING finger ubiquitin E3 ligase. Exp Cell Res 308: 146–155

Krystkowiak I & Davey NE (2017) SLiMSearch: a framework for proteome-wide discovery and annotation of functional modules in intrinsically disordered regions. Nucleic Acids Res 45: W464–W469

Kumar M, Michael S, Alvarado-Valverde J, Mészáros B, Sámano-Sánchez H, Zeke A, Dobson L, Lazar T, Örd M, Nagpal A, et al (2022) The Eukaryotic Linear Motif resource: 2022 release. Nucleic Acids Res 50: D497–D508

Kyte J & Doolittle RF (1982) A simple method for displaying the hydropathic character of a protein. J Mol Biol 157: 105–132

Letunic I, Khedkar S & Bork P (2021) SMART: recent updates, new developments and status in 2020. Nucleic Acids Res 49: D458–D460

Leung AKW, Nagai K & Li J (2011) Structure of the spliceosomal U4 snRNP core domain and its implication for snRNP biogenesis. Nature 473: 536–539

Lu R, Yang P, O'Hare P & Misra V (1997) Luman, a new member of the CREB/ATF family, binds to herpes simplex virus VP16-associated host cellular factor. Mol Cell Biol 17: 5117–5126

Luck K, Charbonnier S & Travé G (2012) The emerging contribution of sequence context to the specificity of protein interactions mediated by PDZ domains. FEBS Lett 586: 2648–2661

Luck K, Kim D-K, Lambourne L, Spirohn K, Begg BE, Bian W, Brignall R, Cafarelli T, Campos-Laborie FJ, Charloteaux B, et al (2020) A reference map of the human binary *protein interactome. Nature 580: 402–408*

Machida YJ, Machida Y, Vashisht AA, Wohlschlegel JA & Dutta A (2009) The deubiquitinating enzyme BAP1 regulates cell growth via interaction with HCF-1. J Biol Chem 284: 34179–34188

Matsuzaki T & Fujiki Y (2008) The peroxisomal membrane protein import receptor Pex3p is directly transported to peroxisomes by a novel Pex19p- and Pex16p-dependent pathway. J Cell Biol 183: 1275–1286

McKinney W (2010) Data structures for statistical computing in python. In Proceedings of the 9th Python in Science Conference pp 56–61. SciPy

Mishra M, Jiang H & Wei Q (2023) New insights on the differential interaction of sulfiredoxin with members of the peroxiredoxin family revealed by protein-protein docking and experimental studies. Eur J Pharmacol 954: 175873

Mistry J, Chuguransky S, Williams L, Qureshi M, Salazar GA, Sonnhammer ELL, Tosatto SCE, Paladin L, Raj S, Richardson LJ, et al (2021) Pfam: The protein families database in 2021. Nucleic Acids Res 49: D412–D419

Miyata T, Miyazawa S & Yasunaga T (1979) Two types of amino acid substitutions in protein evolution. J Mol Evol 12: 219–236

Mo X, Niu Q, Ivanov AA, Tsang YH, Tang C, Shu C, Li Q, Qian K, Wahafu A, Doyle SP, et al (2022) Systematic discovery of mutation-directed neo-protein-protein interactions in cancer. Cell 185: 1974-1985.e12

Mosca R, Céol A & Aloy P (2013) Interactome3D: adding structural details to protein networks. Nat Methods 10: 47–53

Mosca R, Céol A, Stein A, Olivella R & Aloy P (2014) 3did: a catalog of domain-based interactions of known three-dimensional structure. Nucleic Acids Res 42: D374-9

Mourão A, Bonnal S, Soni K, Warner L, Bordonné R, Valcárcel J & Sattler M (2016) Structural basis for the recognition of spliceosomal SmN/B/B' proteins by the RBM5 OCRE domain in splicing regulation. eLife 5

O'Reilly FJ, Graziadei A, Forbrig C, Bremenkamp R, Charles K, Lenz S, Elfmann C, Fischer L, Stülke J & Rappsilber J (2023) Protein complexes in cells by AI-assisted structural proteomics. Mol Syst Biol 19: e11544

ORFeome Collaboration (2016) The ORFeome Collaboration: a genome-scale human ORF-clone resource. Nat Methods 13: 191–192

Parsons JL, Khoronenkova SV, Dianova II, Ternette N, Kessler BM, Datta PK & Dianov GL (2012) Phosphorylation of PNKP by ATM prevents its proteasomal degradation and enhances resistance to oxidative stress. Nucleic Acids Res 40: 11404–11415

Pedregosa F, Varoquaux G, Gramfort A, Michel V, Thirion B, Grisel O, Blondel M, Müller A, Nothman J, Louppe G, et al (2012) Scikit-learn: Machine Learning in Python. arXiv

Persson E & Sonnhammer ELL (2023) InParanoiDB 9: Ortholog Groups for Protein Domains and Full-Length Proteins. J Mol Biol 435: 168001

Schmidt F, Treiber N, Zocher G, Bjelic S, Steinmetz MO, Kalbacher H, Stehle T & Dodt G (2010) Insights into peroxisome function from the structure of PEX3 in complex with a soluble fragment of PEX19. J Biol Chem 285: 25410–25417

Sobti M, Mead BJ, Stewart AG, Igreja C & Christie M (2023) Molecular basis for GIGYF-TNRC6 complex assembly. RNA 29: 724–734

Teufel F, Refsgaard JC, Kasimova MA, Deibler K, Madsen CT, Stahlhut C, Grønborg M, Winther O & Madsen D (2023) Deorphanizing peptides using structure prediction. J Chem Inf Model 63: 2651–2655

Tompa P, Davey NE, Gibson TJ & Babu MM (2014) A million peptide motifs for the molecular biologist. Mol Cell 55: 161–169

Trepte P, Kruse S, Kostova S, Hoffmann S, Buntru A, Tempelmeier A, Secker C, Diez L, Schulz A, Klockmeier K, et al (2018) LuTHy: a double-readout bioluminescence-based two-hybrid technology for quantitative mapping of protein-protein interactions in mammalian cells. Mol Syst Biol 14: e8071

Trepte P, Secker C, Choi SG, Olivet J, Ramos ES, Cassonnet P, Golusik S, Zenkner M, Beetz S, Sperling M, et al (2021) A quantitative mapping approach to identify direct interactions within complexomes. bioRxiv DOI:10.1101/2021.08.25.457734 [PREPRINT]

Trepte P, Secker C, Kostova S, Maseko SB, Choi SG, Blavier J, Minia I, Ramos ES, Cassonnet P, Golusik S, et al (2023) AI-guided pipeline for protein-protein interaction drug discovery identifies a SARS-CoV-2 inhibitor. bioRxiv DOI:10.1101/2023.06.14.544560 [PREPRINT]

Tsaban T, Varga JK, Avraham O, Ben-Aharon Z, Khramushin A & Schueler-Furman O (2022) Harnessing protein folding neural networks for peptide-protein docking. Nat Commun 13: 176

Van Roey K, Gibson TJ & Davey NE (2012) Motif switches: decision-making in cell regulation. Curr Opin Struct Biol 22: 378–385

Varadi M, Anyango S, Deshpande M, Nair S, Natassia C, Yordanova G, Yuan D, Stroe O, Wood G, Laydon A, et al (2022) AlphaFold Protein Structure Database: massively expanding the structural coverage of protein-sequence space with high-accuracy models. Nucleic Acids Res 50: D439–D444

Virtanen P, Gommers R, Oliphant TE, Haberland M, Reddy T, Cournapeau D, Burovski E, Peterson P, Weckesser W, Bright J, et al (2020) SciPy 1.0: fundamental algorithms for scientific computing in Python. Nat Methods 17: 261–272

Wang W, Xia Z-J, Farré J-C & Subramani S (2017) TRIM37, a novel E3 ligase for PEX5-mediated peroxisomal matrix protein import. J Cell Biol 216: 2843–2858

Waskom M (2021) seaborn: statistical data visualization. JOSS 6: 3021

Weatheritt RJ, Jehl P, Dinkel H & Gibson TJ (2012) iELM--a web server to explore short linear motif-mediated interactions. Nucleic Acids Res 40: W364-9

Zhao G, Li K, Li B, Wang Z, Fang Z, Wang X, Zhang Y, Luo T, Zhou Q, Wang L, et al (2020) Gene4Denovo: an integrated database and analytic platform for de novo mutations in humans. Nucleic Acids Res 48: D913–D926

Zhu Y, Wang WL, Yu D, Ouyang Q, Lu Y & Mao Y (2018) Structural mechanism for nucleotide-driven remodeling of the AAA-ATPase unfoldase in the activated human 26S proteasome. Nat Commun 9: 1360

Figure legends

Figure 1. Benchmarking and application of AF for DMI interface prediction using minimal interacting fragments.
A Proportion of structures of DMIs predicted by AF to different levels of accuracy. Categories were defined based on motif RMSD cutoffs. **B** Accuracy of AF DMI predictions stratified according to the annotated functional categories of DMIs in the ELM DB. DEG=degron, DOC=docking, LIG=ligand, TRG=targeting, MOD=modification. **C** Accuracy of AF DMI predictions stratified according to the secondary structure element formed by the motif in the solved structure. **D** Accuracy of AF DMI predictions stratified according to the method used to solve the structures in the benchmark dataset. **E** Area under the Receiver Operating Characteristics Curve (AUROC) for different metrics using the DMI or DDI benchmark dataset as positive reference and the following different random reference sets: Left (DMI), 1 mutation introduced in conserved motif position; middle-left (DMI), 2 mutations introduced in conserved motif position, middle-right (DMI), random domain-motif pairs from reshuffling of pairings from positive DMI reference dataset; right (DDI), random domain-domain pairs from reshuffling pairings from positive DDI reference dataset. **F** Superimposition of AF structural model for motif class MOD_SUMO_rev_2 (orange) with homologous solved structure (PDB:1KPS) from motif class MOD_SUMO_for_1 (blue). The motif sequence used for prediction is indicated at the bottom, colored by pLDDT (dark blue=highest pLDDT). **G** Superimposition of AF structural model for motif class CLV_C14_Caspase3-7 (orange) with homologous structure (PDB:5IAN) solved with a peptide-like inhibitor (blue). The motif sequence used for prediction is indicated at the bottom, colored by pLDDT (dark blue=highest pLDDT). **H** AF prediction of a LIG_HCF-1_HBM_1 motif in CREBZF (orange) binding to the beta-propeller Kelch domain of HCFC1 (gray). Mutated domain residues for experimental testing are colored in green. **I** Close up on the interface shown between CREBZF and HCFC1 from H. Coloring is the same as in H. Key conserved motif residues are drawn as sticks. Mutated residues in the domain and motif for experimental testing are labeled. **J** BRET titration curves are shown for wildtype interactions and mutant constructs for CREBZF-HCFC1 pairs for two biological replicates, each with three technical replicates. Protein acceptor over protein donor expression levels are plotted on the x-axis determined from fluorescence and luminescence measurements, respectively.

Figure 2. Effect of protein fragment extensions on the accuracy of AF predictions.
A Schematic of motif and domain sequence extensions and heatmap showing the fold change in motif RMSD before and after extension where positive values indicate improved predictions from extension and negative values indicate worse prediction outcomes. 31 DMI structures from the positive benchmark dataset were selected for this extension analysis. **B** Heatmap of the average model confidence for combinations of different motif and domain sequence extensions. Extensions like in A. **C** Optimal cutoffs derived for different metrics from ROC analysis for benchmarking AF with predictions using different combinations of motif and domain extensions from the reference dataset used in A and random pairings of domain and motif sequences. pLDDT-related metrics were divided by 100 for visualization purposes. **D** Scatterplot of motif RMSDs using minimal motif sequences (extension 0) vs extending motif sequences once by the length of the motif to the left and right (extension 1). Labels in the plot refer to figure panels with examples of how slight extensions improved AF prediction accuracies. Sizes of the dots in the plot reflect the difference in RMSD between the two extensions. **E-G** Superimposition of the structural model of the minimal (left, orange) or extended (right, yellow) motif sequence with the solved structure (motif in blue) for three

different motif classes as indicated on the top of each panel. The motif sequence from the solved structure is indicated at the bottom of each panel. Motif residues are underlined, motif residues not resolved in the structure have a gray background. Sticks indicate the motif residues, domain surfaces are shown in gray based on experimental structures.

Figure 3. AF prediction and experiments on PPIs connecting NDD proteins.
A Schematic showing fragmentation approach. **B** Fraction of fragment pairs with structural model scoring above thresholds for 20 random protein pairs. Numbers on top of the bars indicate the total number of fragment pairs predicted for each random protein pair. **C** AF prediction outcome on 67 HuRI PPIs connecting NDD proteins. **D** PPI networks illustrating AF prediction outcomes and experimental retesting of PPIs in BRET assay. **E** Number of PPIs connecting NDD proteins with structural models at indicated pDockQ cutoffs from (Burke *et al*, 2023) grouped based on AF prediction outcomes using the fragmentation approach as shown in C. **F** cBRET, total luminescence, and fluorescence for 28 PPIs connecting NDD proteins that were tested in the BRET assay. Luminescence and fluorescence measurements indicate expression levels of NL and mCit fusion proteins, respectively. Black horizontal lines indicate expression level and PPI detection cutoffs. The gray vertical line separates the detected (left) from undetected PPIs. Protein pairs in bold indicate those selected for interface validation via site-directed mutagenesis.

Figure 4. Verification of interface predictions for TRIM37-PNKP and ESRRG-PSMC5.
A Schematic of the domain architecture of PNKP and TRIM37 with indication of top predicted interfaces. Numbers in blue indicate the average motif interface pLDDT for the respective interface. Roman numbering refers to structural models in B and C. **B** Structural model of interface i shown in A with labeled residues that were mutated. **C** Structural model of interface ii shown in A. **D** BRET titration curves are shown for wildtype interaction and mutants for two biological replicates, each with three technical replicates. Protein acceptor over protein donor expression levels are plotted on the x-axis determined from fluorescence and luminescence measurements, respectively. The BRET trajectory could not be fitted because of an unusual saturation behavior. **E** Schematic of the domain architecture of ESRRG and PSMC5 with indication of top predicted interfaces. Numbers in blue indicate the average motif interface pLDDT for the respective interface. Roman numbering refers to structural models in F and G. **F** Structural model of interface iii shown in E with labeled residues that were mutated. **G** Structural model of interface iv shown in E. **H** BRET titration curves are shown for wildtype interaction and mutants of ESRRG-PSMC5 pairs for two biological replicates, each with three technical replicates. Protein acceptor over protein donor expression levels are plotted on the x-axis determined from fluorescence and luminescence measurements, respectively. In panels B, C, F, and G motif sequences are indicated at the bottom. Gray letters indicate residues not predicted to bind.

Figure 5. Verification of interface predictions for STX1B-FBXO28, STX1B-VAMP2, PEX3-PEX19, and PEX3-PEX16. **A** Schematic of the domain architecture of STX1B, FBXO28, and VAMP2 with indication of top predicted interfaces. Numbers in blue indicate the average motif interface pLDDT or model confidence (DDI) for the respective interface. Roman numbering refers to structural models in B, C, Fig S8E, and Fig S8I. **B** Structural model of interface iii shown in A with tested pathogenic mutations labeled and colored in green. **C** Structural model of interface iv shown in A. In panel B and C, the chains are color-coded according to the colors of the domains in A. **D-F** BRET titration curves are shown for wildtype interactions and deletion

constructs for two biological replicates, each with three technical replicates. Protein acceptor over protein donor expression levels are plotted on the x-axis determined from fluorescence and luminescence measurements, respectively. **G** Schematic of the domain architecture of PEX3, PEX19, and PEX16 with indication of top predicted interfaces. Numbers in blue indicate the average motif interface pLDDT for the respective interface. Roman numbering refers to structural models in H, J, and Fig S9A. Region vi covers residues 1-170, which includes the previously reported N-terminal motif as well as three putative motifs suggested by the AF models. **H** Superimposition of structural models of interface vi and vii on the PEX3 domain. Note that modeling smaller fragments of PEX19 generates alternative interactions with the binding sites. **I** BRET titration curves are shown for wildtype interaction and mutants of PEX3-PEX19 pairs for three technical replicates. Protein acceptor over protein donor expression levels are plotted on the x-axis determined from fluorescence and luminescence measurements, respectively. The left plot displays mutants aimed at disrupting binding between PEX3-PEX19 while the right plot displays mutants aimed at disrupting the PEX3-PEX16 PPI why binding between PEX3-PEX19 should not be altered. **J** Structural model of interface vii shown in G. **K** BRET values with subtracted bleedthrough for PEX3-PEX16 wildtype and various mutated constructs. Three technical replicates are shown. **L** Proposed model for how the trimeric complex of PEX3, PEX19, and PEX16 might assemble at the peroxisomal membrane.

Figure 6. Verification of interface predictions for SNRPB-GIGYF1. A Schematic of the domain architecture of SNRPB and GIGYF1 with indication of top predicted interfaces. Numbers in blue indicate the average motif interface pLDDT for the respective interface. Roman numbering refers to structural models in B and C. **B** Structural model of interface i shown in A with tested domain mutations labeled and colored green. The motif sequence is indicated at the bottom. **C** Structural model of interface ii shown in A (left) and in comparison a solved structure (PDB:4WZJ) of the Sm ring complex (right) bound to RNA (orange). The LSM domain of SNRPB is shown in cyan. The position of the predicted motif (left) or neighboring LSM domain of SNRPD3 (right) are indicated in gold. Black circles indicate the predicted interface in the model and corresponding interface in the complex on the LSM domain of SNRPB. **D** Solved structure (PDB:7RUQ) of the GYF domain of GIGYF1 bound to a proline-rich motif in TNRC6C. **E-F** BRET titration curves are shown for wildtype interactions, deletion constructs of SNRPB, and single point mutants in GIGYF1 for two biological replicates, each with three technical replicates. Protein acceptor over protein donor expression levels are plotted on the x-axis determined from fluorescence and luminescence measurements, respectively. **G** Cropped immunoblot of input (5%) and HA antibody immunoprecipitation (IP) performed in parental HEK cells (empty, untagged negative control), Snrpb(full-length, 1-231)-2xHA-mNeonGreen, Snrpb(1-190)-2xHA-mNeonGreen expressed from a single locus in Flp-In™ T-REx™ 293 Cell Lines. The HA antibody was used for detecting the immunoprecipitated Snrpb-proteins, endogenous GIGYF1 was detected with GIGYF1 antibody, GAPDH serves as a loading and negative-IP control. The experiment was performed twice with equivalent outcome, one representative experiment is shown.

Figure 1

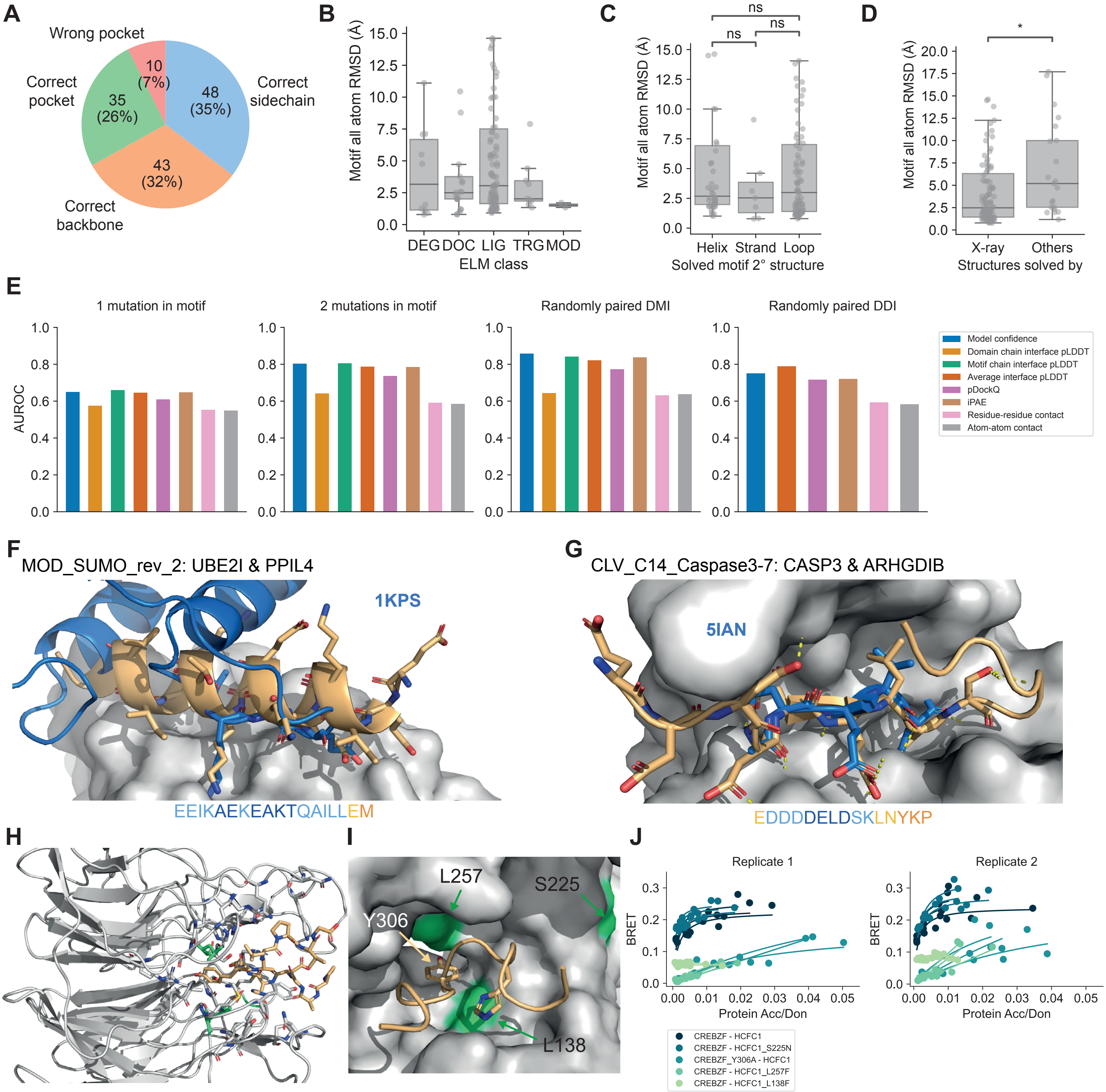
A
Wrong pocket
10 (7%)
Correct pocket
35 (26%)
48 (35%)
Correct sidechain
43 (32%)
Correct backbone
B
Motif all atom RMSD (Å)
0.0 2.5 5.0 7.5 10.0 12.5 15.0
DEG DOC LIG TRG MOD
ELM class
C
ns
ns
ns
Motif all atom RMSD (Å)
0.0 2.5 5.0 7.5 10.0 12.5 15.0
Helix Strand Loop
Solved motif 2° structure
D
*
Motif all atom RMSD (Å)
0.0 2.5 5.0 7.5 10.0 12.5 15.0 17.5 20.0
X-ray Others
Structures solved by
E
1 mutation in motif
2 mutations in motif
Randomly paired DMI
Randomly paired DDI
AUROC
0.0 0.2 0.4 0.6 0.8 1.0
Model confidence
Domain chain interface pLDDT
Motif chain interface pLDDT
Average interface pLDDT
pDockQ
iPAE
Residue-residue contact
Atom-atom contact
F
MOD_SUMO_rev_2: UBE2I & PPIL4
1KPS
EEIKAEKEAKTQAILLEM
G
CLV_C14_Caspase3-7: CASP3 & ARHGDIB
5IAN
EDDDDELDSKLNYKP
H
I
L257
S225
Y306
L138
J
Replicate 1
Replicate 2
BRET
0.0 0.1 0.2 0.3
0.00 0.01 0.02 0.03 0.04 0.05
Protein Acc/Don
CREBZF - HCFC1
CREBZF - HCFC1_S225N
CREBZF_Y306A - HCFC1
CREBZF - HCFC1_L257F
CREBZF - HCFC1_L138F

Figure 2

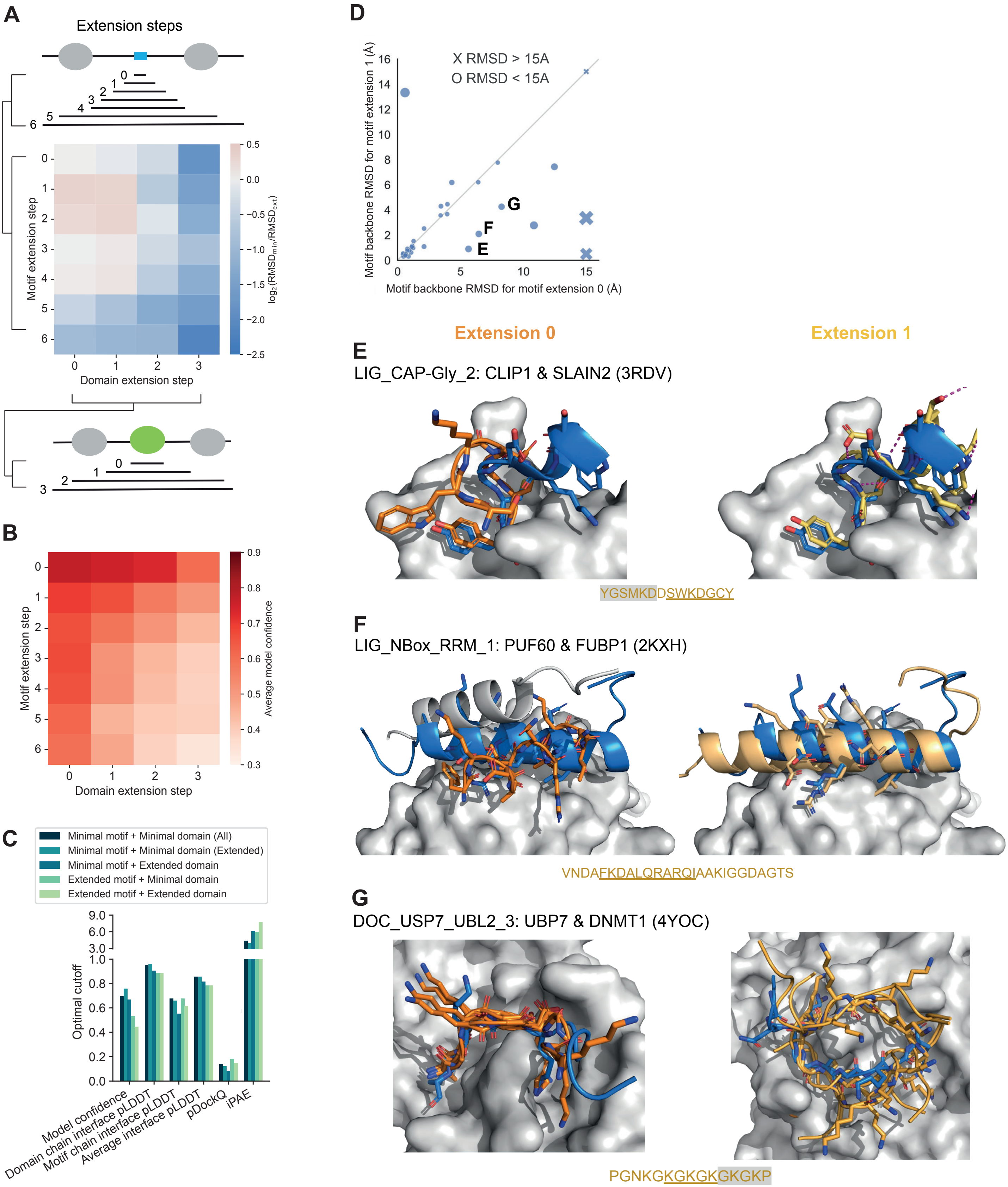
A
Extension steps
0
1
2
3
4
5
6
Motif extension step
Domain extension step
log₂(RMSD_min/RMSD_ext)
0.5
0.0
−0.5
−1.0
−1.5
−2.0
−2.5
B
Motif extension step
Domain extension step
Average model confidence
0.9
0.8
0.7
0.6
0.5
0.4
0.3
C
Minimal motif + Minimal domain (All)
Minimal motif + Minimal domain (Extended)
Minimal motif + Extended domain
Extended motif + Minimal domain
Extended motif + Extended domain
Optimal cutoff
9.0
6.0
3.0
1.0
0.8
0.6
0.4
0.2
0.0
Model confidence
Domain chain interface pLDDT
Motif chain interface pLDDT
Average interface pLDDT
pDockQ
iPAE
D
X RMSD > 15A
O RMSD < 15A
Motif backbone RMSD for motif extension 1 (Å)
Motif backbone RMSD for motif extension 0 (Å)
0
2
4
6
8
10
12
14
16
5
10
15
G
F
E
Extension 0
Extension 1
E
LIG_CAP-Gly_2: CLIP1 & SLAIN2 (3RDV)
YGSMKDDSWKDGCY
F
LIG_NBox_RRM_1: PUF60 & FUBP1 (2KXH)
VNDAFKDALQRARQIAAKIGGDAGTS
G
DOC_USP7_UBL2_3: UBP7 & DNMT1 (4YOC)
PGNKGKGKGKGKGKP

Figure 3

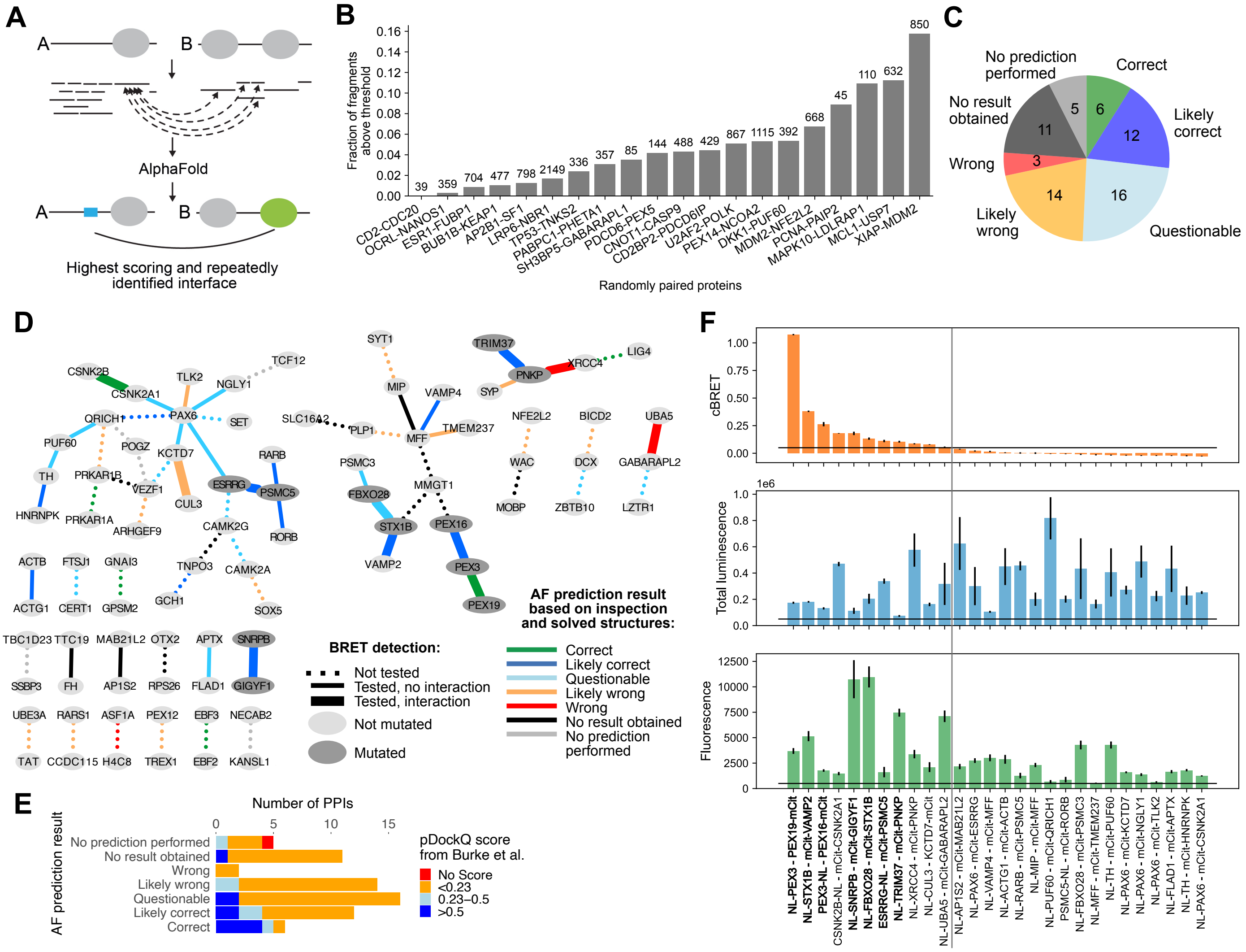
A
A
B
AlphaFold
A
B
Highest scoring and repeatedly identified interface
B
Fraction of fragments above threshold
Randomly paired proteins
39 359 704 477 798 2149 336 357 85 144 488 429 867 1115 392 668 45 110 632 850
CD2-CDC20
OCRL-NANOS1
ESR1-FUBP1
BUB1B-KEAP1
AP2B1-SF1
LRP6-NBR1
TP53-TNKS2
PABPC1-PHETA1
SH3BP5-GABARAPL1
PDCD6-PEX5
CNOT1-CASP9
CD2BP2-PDCD6IP
U2AF2-POLK
PEX14-NCOA2
DKK1-PUF60
MDM2-NFE2L2
PCNA-PAIP2
MAPK10-LDLRAP1
MCL1-USP7
XIAP-MDM2
C
No prediction performed 5
Correct 6
Likely correct 12
Questionable 16
Likely wrong 14
Wrong 3
No result obtained 11
D
CSNK2B CSNK2A1 TLK2 NGLY1 TCF12 QRICH1 PAX6 SET PUF60 POGZ KCTD7 PRKAR1B VEZF1 CUL3 TH HNRNPK PRKAR1A ARHGEF9 ESRRG PSMC5 RARB RORB CAMK2G TNPO3 CAMK2A GCH1 SOX5
SYT1 MIP VAMP4 TRIM37 PNKP XRCC4 LIG4 SYP SLC16A2 PLP1 MFF TMEM237 PSMC3 FBXO28 MMGT1 STX1B PEX16 VAMP2 PEX3 PEX19
NFE2L2 WAC MOBP BICD2 DCX ZBTB10 UBA5 GABARAPL2 LZTR1
ACTB ACTG1 FTSJ1 CERT1 GNAI3 GPSM2
TBC1D23 SSBP3 TTC19 FH MAB21L2 AP1S2 OTX2 RPS26 APTX FLAD1 SNRPB GIGYF1
UBE3A TAT RARS1 CCDC115 ASF1A H4C8 PEX12 TREX1 EBF3 EBF2 NECAB2 KANSL1
BRET detection:
Not tested
Tested, no interaction
Tested, interaction
Not mutated
Mutated
AF prediction result based on inspection and solved structures:
Correct
Likely correct
Questionable
Likely wrong
Wrong
No result obtained
No prediction performed
E
Number of PPIs
0 5 10 15
AF prediction result
No prediction performed
No result obtained
Wrong
Likely wrong
Questionable
Likely correct
Correct
pDockQ score from Burke et al.
No Score
<0.23
0.23–0.5
>0.5
F
cBRET
Total luminescence
1e6
Fluorescence
NL-PEX3 - PEX19-mCit
NL-STX1B - mCit-VAMP2
PEX3-NL - PEX16-mCit
CSNK2B-NL - mCit-CSNK2A1
NL-SNRPB - mCit-GIGYF1
NL-FBXO28 - mCit-STX1B
ESRRG-NL - mCit-PSMC5
NL-TRIM37 - mCit-PNKP
NL-XRCC4 - mCit-PNKP
NL-CUL3 - KCTD7-mCit
NL-UBA5 - mCit-GABARAPL2
NL-AP1S2 - mCit-MAB21L2
NL-PAX6 - mCit-ESRRG
NL-VAMP4 - mCit-MFF
NL-ACTG1 - mCit-ACTB
NL-RARB - mCit-PSMC5
NL-MIP - mCit-MFF
NL-PUF60 - mCit-QRICH1
PSMC5-NL - mCit-RORB
NL-FBXO28 - mCit-PSMC3
NL-MFF - mCit-TMEM237
NL-TH - mCit-PUF60
NL-PAX6 - mCit-KCTD7
NL-PAX6 - mCit-NGLY1
NL-PAX6 - mCit-TLK2
NL-FLAD1 - mCit-APTX
NL-TH - mCit-HNRNPK
NL-PAX6 - mCit-CSNK2A1

Figure 4

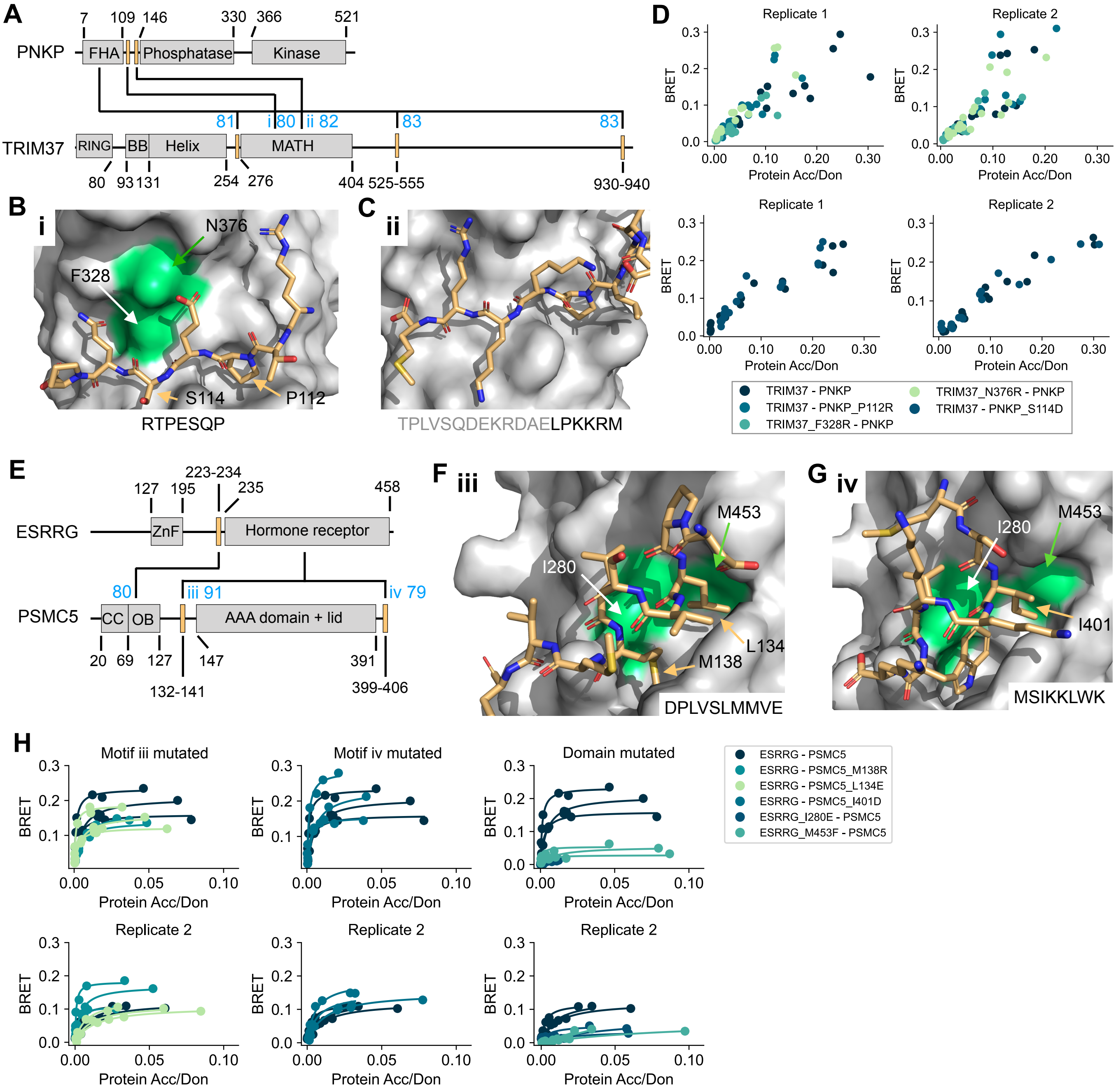
A
PNKP
7
109
146
330
366
521
FHA
Phosphatase
Kinase
TRIM37
RING
BB
Helix
MATH
81
i 80
ii 82
83
83
80
93
131
254
276
404
525-555
930-940
B
i
N376
F328
S114
P112
RTPESQP
C
ii
TPLVSQDEKRDAELPKKRM
D
Replicate 1
Replicate 2
BRET
Protein Acc/Don
0.0
0.1
0.2
0.3
0.00
0.10
0.20
0.30
TRIM37 - PNKP
TRIM37 - PNKP_P112R
TRIM37_F328R - PNKP
TRIM37_N376R - PNKP
TRIM37 - PNKP_S114D
E
ESRRG
127
195
223-234
235
458
ZnF
Hormone receptor
PSMC5
CC
OB
AAA domain + lid
80
iii 91
iv 79
20
69
127
147
132-141
391
399-406
F
iii
M453
I280
L134
M138
DPLVSLMMVE
G
iv
M453
I280
I401
MSIKKLWK
H
Motif iii mutated
Motif iv mutated
Domain mutated
Replicate 2
BRET
Protein Acc/Don
0.0
0.1
0.2
0.3
0.00
0.05
0.10
ESRRG - PSMC5
ESRRG - PSMC5_M138R
ESRRG - PSMC5_L134E
ESRRG - PSMC5_I401D
ESRRG_I280E - PSMC5
ESRRG_M453F - PSMC5

Figure 5

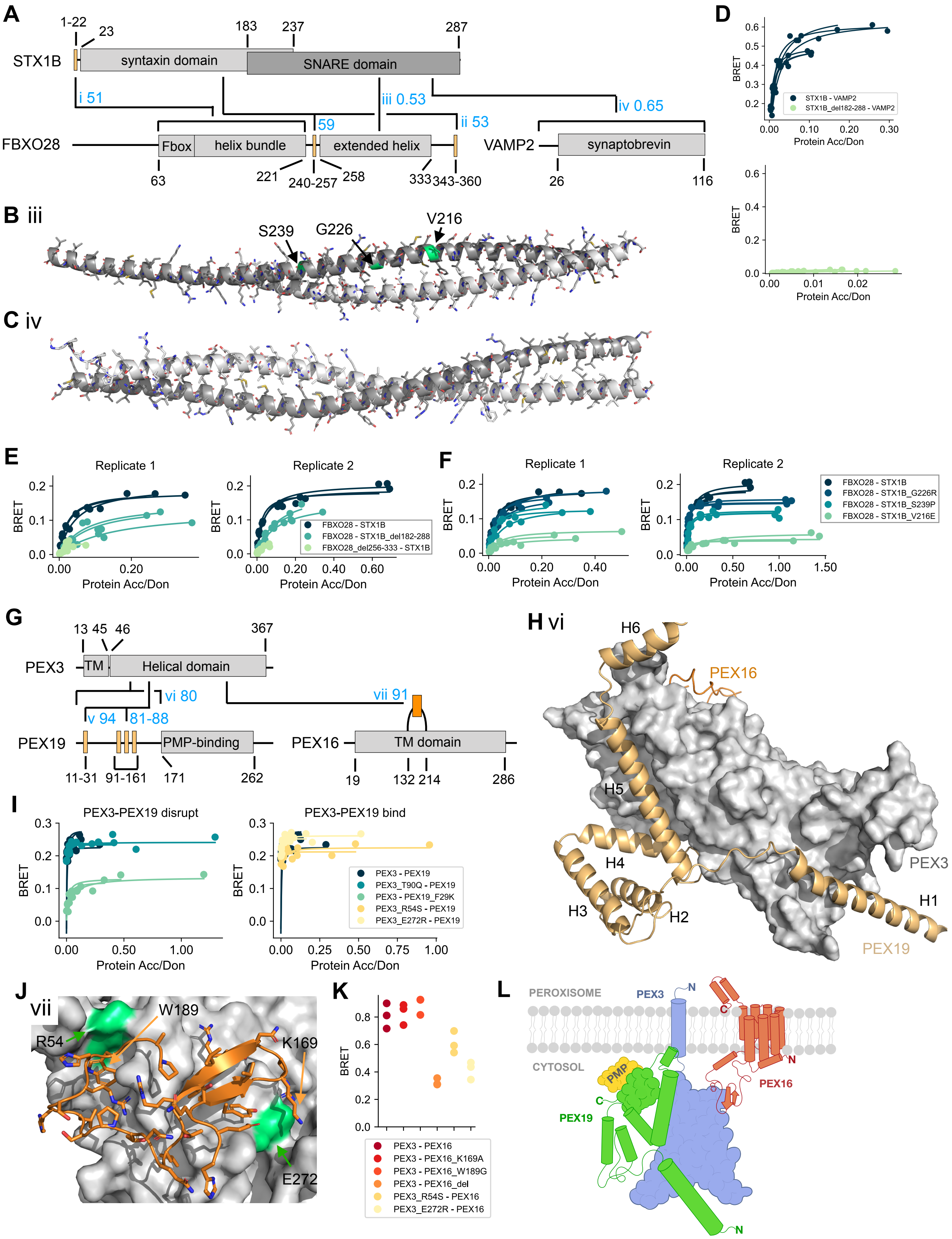
A
1-22
23
183
237
287
STX1B
syntaxin domain
SNARE domain
i 51
iii 0.53
iv 0.65
59
ii 53
FBXO28
Fbox
helix bundle
extended helix
VAMP2
synaptobrevin
63
221
240-257
258
333
343-360
26
116
B iii
S239
G226
V216
C iv
D
BRET
0.6
0.5
0.4
0.3
0.2
STX1B - VAMP2
STX1B_del182-288 - VAMP2
0.00
0.10
0.20
0.30
Protein Acc/Don
0.6
0.4
0.2
0.0
0.00
0.01
0.02
Protein Acc/Don
E
Replicate 1
Replicate 2
BRET
0.2
0.1
0.0
0.00
0.20
0.40
0.60
Protein Acc/Don
FBXO28 - STX1B
FBXO28 - STX1B_del182-288
FBXO28_del256-333 - STX1B
F
Replicate 1
Replicate 2
0.00
0.20
0.40
0.50
1.00
1.50
Protein Acc/Don
FBXO28 - STX1B
FBXO28 - STX1B_G226R
FBXO28 - STX1B_S239P
FBXO28 - STX1B_V216E
G
13
45
46
367
PEX3
TM
Helical domain
vi 80
vii 91
v 94
81-88
PEX19
PMP-binding
PEX16
TM domain
11-31
91-161
171
262
19
132
214
286
H vi
H6
PEX16
H5
H4
H3
H2
H1
PEX3
PEX19
I
PEX3-PEX19 disrupt
PEX3-PEX19 bind
BRET
0.3
0.2
0.1
0.0
0.00
0.25
0.50
0.75
1.00
Protein Acc/Don
PEX3 - PEX19
PEX3_T90Q - PEX19
PEX3 - PEX19_F29K
PEX3_R54S - PEX19
PEX3_E272R - PEX19
J vii
W189
R54
K169
E272
K
BRET
0.8
0.6
0.4
0.2
0.0
PEX3 - PEX16
PEX3 - PEX16_K169A
PEX3 - PEX16_W189G
PEX3 - PEX16_del
PEX3_R54S - PEX16
PEX3_E272R - PEX16
L
PEROXISOME
PEX3
N
C
N
CYTOSOL
PMP
PEX16
C
PEX19
N

Figure 6

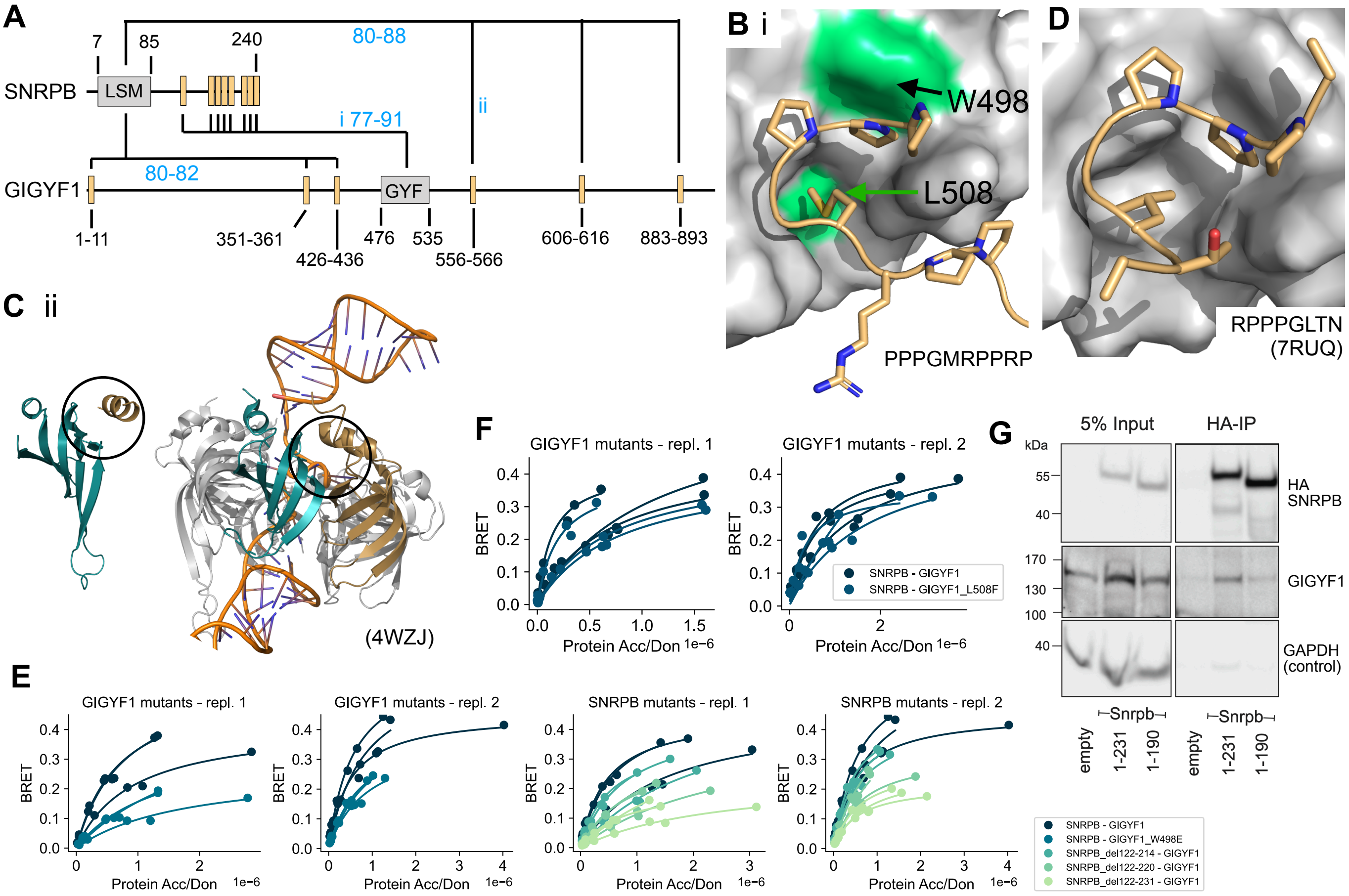
A
7
85
240
80-88
SNRPB
LSM
ii
i 77-91
80-82
GIGYF1
GYF
1-11
351-361
426-436
476
535
556-566
606-616
883-893
B i
W498
L508
PPPGMRPPPRP
D
RPPPGLTN
(7RUQ)
C ii
(4WZJ)
F
GIGYF1 mutants - repl. 1
GIGYF1 mutants - repl. 2
BRET
Protein Acc/Don 1e−6
SNRPB - GIGYF1
SNRPB - GIGYF1_L508F
G
kDa
5% Input
HA-IP
55
40
HA
SNRPB
170
130
100
GIGYF1
GAPDH
(control)
Snrpb
empty
1-231
1-190
E
GIGYF1 mutants - repl. 1
GIGYF1 mutants - repl. 2
SNRPB mutants - repl. 1
SNRPB mutants - repl. 2
BRET
Protein Acc/Don 1e−6
SNRPB - GIGYF1
SNRPB - GIGYF1_W498E
SNRPB_del122-214 - GIGYF1
SNRPB_del122-220 - GIGYF1
SNRPB_del122-231 - GIGYF1